Open Research Online

Plasma engineering of graphene

Journal Item

Version: Accepted Manuscript

oro.open.ac.uk

Plasma engineering of graphene

A. Dey,[1] A. Chroneos,[2,3] N.S Braithwaite [4] , Ram P. Gandhiraman [5] and S. Krishnamurthy*[1, a)]

[1]*Materials Engineering, The Open University, Milton Keynes, MK7 6AA, United Kingdom*
[2]*Faculty of Engineering, Environment and Computing, Coventry University, Priory Street, Coventry CV1 5FB, United Kingdom*
[3]*Department of Materials, Imperial College London, London SW7 2AZ, United Kingdom*
[4]*Department of Physical Sciences, The Open University, Milton Keynes, MK7 6AA, United Kingdom*
[5]*Universities Space Research Association, NASA Ames Research Center, Moffett Field, CA 94035, United States*

Abstract

Recently, there have been enormous efforts to tailor the properties of graphene. These improved properties extend the prospect of graphene for a broad range of applications. Plasmas find applications in various fields including materials science and have been emerging in the field of nanotechnology. This review focuses on different plasma functionalization processes of graphene and its oxide counterpart. The review aims at the advantages of plasma functionalization over the conventional doping techniques. Selectivity and controllability of the plasma techniques opens up future pathways for large scale, rapid functionalization of graphene for advanced applications. We also emphasize on atmospheric pressure plasma jet as the future prospect of plasma based functionalization processes.

Keywords: *review graphene, doping, Plasma, Atmospheric pressure, plasma functionalization.*

Table of contents:

I. Introduction

Graphene, the 2-D allotrope of carbon, has gained significant attention, since it was isolated in 2004 by Geim and Novoselov.[1] Graphene is one atom thick honeycomb lattice of sp^2 bonded carbon atoms and is the elementary unit of all the graphite allotropes. When wrapped it forms 0D dimensional fullerenes, after rolling it becomes 1D dimensional nanotubes and when stacked forms 3D dimensional graphite.

Graphene is renowned for its remarkable electronic and optical properties. The most interesting properties are its high thermal conductivity (5000 W/mK) [2], extremely high room temperature mobility of charge carriers (250,000 cm^2·V^{-1}·s^{-1}) [3] which exceeds its theoretical predicted value of 200,000 cm^2·V^{-1}·s^{-1} ,[4] high surface area (2630 m^2/g) [5], optical absorption of $\pi\alpha \approx 2.3\%$ [6] and ability to withstand extremely high

current densities. [7] These superior electrical and optical properties arise from the

unique band structure of graphene.[8] Density of states at the Fermi level is zero for

undoped graphene. The charge carriers in graphene behave as massless Dirac fermions

and its conductivity never falls below a minimum value. Graphene also exhibits

anomalous and fractional quantum hall effect.[9] These electronics properties have been

determined to be superior when compared to many traditional materials used presently

in the electronics industry. Other properties include its high mechanical stiffness

(Young's modulus of 1 TPa) [10], complete impermeability to gasses[11] and its ease to

functionalization.[12] Owing to its unprecedented properties graphene is potentially

important in the field of flexible electronics, super-fast transistors, photonics, energy

(generation and storage), sensors and biology.[13,14,15,16]

Different techniques have been successfully implemented to tailor properties of

graphene and graphene oxide (GO). As graphene is a zero band gap semimetal, band

gap opening plays a crucial role in its application in various electronic and

optoelectronic devices especially in logic circuits. Chemical modification of graphene

has been the most widely used technique. This involves doping[17] and surface

functionalization.[18] The presence of electronegative oxygen functionalities can lead to

its *p*-type behaviour while the substitution of electropositive atoms such as nitrogen

into its lattice, *n*-type behaviour can be achieved.[19] Absorption of different metals [20,21],

gasses [22] and organic molecules [23,24] can also modulate the electronic properties of

graphene. Morphology plays an important role in the graphene properties. Exfoliation

of graphite flakes led to graphene nanosheets proposed to overcome the hydrophobic

nature of graphene. This lead to the large-scale production of aqueous dispersions of

graphene.[25,26] One dimensional graphene nanoribbons (GNRs) with width narrower

than 10 nm exhibit semiconducting behaviour opening the possibility of ultrafast

graphene field effect transistors.[27,28] Edge regions of graphene sheets play a key role in

determining its electronic properties. Zig-Zag edges show higher chemical reactivity owing to lesser thermodynamic stability with respect to arm-chair edges.[29] Zero-dimensional graphene quantum dots (GQDs) exhibit pronounced edge effects and quantum confinement in comparison to GNRs in the same size regime. [30,31] Due to these GQDs exhibit superior optical properties than GNRs. Band gap opening has also been seen in strained graphene lattices, as a consequence of breaking of sub-lattice symmetry.[32] It was also determined that creating ripples on the graphene lattice by basic thermal treatments could lead to stoichiometric functionalization of graphene. This is because strained areas in the lattice act as preferential sites for reactions.

GO can be considered as a promising alternative to graphene and is in essence the monolayer of graphitic oxide. It can be produced in large scale from low cost graphite powder.[33,34] The history of graphite powder extends back to year 1859 when British chemist B.C Brodie investigated the chemistry of graphite oxide.[35] Brodie determined the chemical composition of graphite oxide and determined it is dispersible in basic water. His reaction involved "chlorate of potash" (potassium chlorate, $KClO_3$), graphite and concentrated nitric acid. The most attractive property of GO is that it can form stable dispersion in variety of solvents compared to graphene, which is highly hydrophobic.[25] Enabling it to be appealing for cheap, solution processed flexible electronic devices.[34]

The oxygen containing functional groups in GO have a profound influence on its optical, electronic, mechanical and electrochemical properties. There have been extensive studies carried out to understand the structure of GO. Numerous models have been suggested to depict the structure of GO.[36] According to these models the basal plane of GO is decorated with hydroxyl and epoxy functional groups. While small

amounts of carboxyl, carbonyl, phenol groups occupy the sheet edges. The polar

oxygen groups render it highly hydrophilic. This enables GO to interact with a varied range of organic, inorganic materials via covalent and ionic bonds. Moreover GO is an electronically hybrid material. The sites with sp^2 carbon (π states) are conductive while the C-O sp^3 sites (σ states) have a large band gap. Thus by adjusting the ratio between sp^2 and sp^3 domains, GO can be transformed from insulator to a semiconductor and even to graphene like semimetal.[37] Reduction of GO is usually carried out through chemical and thermal processes to achieve properties alike of graphene. The defects created due to these oxygen functional groups reduce the conductivity of GO sheets and in turn makes it more electroactive. Thus finding applications in biosensing and electrochemical systems. [38] All these properties makes RGO/GO, a suitable alternative to graphene for various applications.[39]

II.   Introduction to plasma technology

Plasma, often considered as the fourth state of matter, is a gas of charged particles. Plasma can be generated by heating a gas or by applying strong electromagnetic fields. The applied energy ionizes the gas by dissociating the molecular bonds. The ionized gas contains equal densities of oppositely charged particles (electrons and ions) rendering the gas neutral. These charged particles make the plasma electrically conductive. Plasma can be classified into different categories which are listed below: [40]

- ❖ Operating pressure

  - Low pressure plasma

  - Atmospheric pressure plasma

- ❖ Thermodynamics
    - Thermal plasmas, which are in thermodynamic equilibrium state. ($T_{\text{electron}} \approx T_{\text{ion}} \approx T_{\text{gas}}$)
    - Non- thermal plasma or non-equilibrium plasma ($T_{\text{electron}} \gg T_{\text{ion}} \approx T_{\text{gas}}$)
- ❖ Temperature
    - Low temperature plasma where temperature of the plasma is less than 2000 K.
    - High temperature plasma where temperature of the plasma is more than 2000 K.
- ❖ Generation
    - Microwave Discharge (300 MHz ≤ f ≤ 300 GHz)
    - Radio frequency discharge (ideally 13.56 MHz)
    - DC discharge
    - Dielectric barrier discharge
    - Corona discharge
    - Electric arc
    - Hollow cathode discharge
    - Electron beam
    - Plasma torch
    - Alternating current

Non-thermal plasmas have found applications in the field of materials processing for the past fifty years. One of the major advantages of non-thermal plasma is that it consists of abundant chemically active species, for reaction with different surfaces. Thus plasma processing can provide unique opportunities for low temperature material processing which is by far better than the other non-destructive techniques. Presently there has been an increasing interest for atmospheric pressure plasmas in materials processing, as it does not require the sophisticated vacuum equipment with respect to the conventional vacuum based plasma systems. This reduces the material processing cost. Figure 1 illustrates the applicability of various plasma processes in comparison to

material processing cost.[41] Atmospheric pressure plasma jets (APPJ) have evolved as a

technique of significant practical importance. This is because the plasma jets are not

restricted within the dimensions of the electrodes. APPJs consist of charged particles,

neutral metastable species, radicals and radiations in the UV and visible regions.[42] The

capabilities of APPJs have been realised extensively for biomedical applications. For

example, Larousi et al.[43] demonstrated the potential of APPJ by killing various types

of bacteria. The low cross section of the jet resulted in a localised effect. This

illustrates the advantage of selectivity involved with this process. This low temperature

process can be used to sterilize medical equipment, which is sensitive to heat. It also

finds applications in the field of food safety because of its ability to deactivate bacterial

growth. The active species present in APPJ can change the wettability of surfaces.[44]

APPJ with extremely low concentration of oxygen mixed with an inert gas can be used

for surface cleaning purposes. A recent review by Penkov et al.[45] provides a detailed

overview on the various applications of APPJs. Clearly APPJs possesses an advantage

over other conventional techniques including vacuum based plasma technologies. Its

key features are simplicity of use, low cost, ease to design and minimal power

consumption.[46] It can prove to be a powerful tool in the field of surface engineering

and functionalization of the 2 dimensional materials and the present review is intended

to justify this claim.

III. Plasma in Carbon Nanotechnology

Carbon based nanomaterials have empowered the world of nanotechnology

with their fascinating properties. A prodigious amount of research and

commercialisation of technology over the past decade or so and the new forms of

carbon and its properties makes these materials unique and ever interesting. For

example, new exciting properties have continued to emerge from amorphous carbon, DLC (diamond like carbon) to graphene. Carbon nanotubes (CNT) have been a major focus of attraction to the scientific world of carbon until the discovery of graphene whereas hard carbon coatings continue to be in spotlight for engineering community. (Refer to Figure 2) There are numerous research articles and review articles on carbon nanotubes. [47–50]

Low temperature non-thermal plasmas have been extensively used in the field of materials processing for the past three decades. These plasmas have been successfully implemented for processing (synthesis and functionalization) of nanomaterials. They are also very significant for the silicon-integrated chip (IC) manufacturing.[51] The techniques of reactive ion etching (RIE) and plasma enhanced chemical vapour deposition (PECVD) are of utmost importance for semiconductor processing. With its accomplishments in silicon industry, applications of plasma have been broadened to carbon nanomaterials (CNT and Graphene).[52] PECVD has emerged as the alternative to high temperature CVD processes for the synthesis of CNT and graphene. Recent studies by Meyyappan [53] and Neyts [54] present a comprehensive review on PECVD growth of CNT along with the advantages of this technique. PECVD has also been successfully implemented to dope CNT and graphene. [55,56]

Plasma based techniques have been predominantly applied to the initial synthesis of carbon-based materials rather than post processing. Plasma also has considerable potential for post synthesis functionalization of carbon based materials. Plasma discharges can allow the fixation of different chemical species of the same element to the graphene structure. Selectivity associated with plasma has opened new dimensions in functionalising graphene in terms of creating definite structural defects

and precision in doping. In the forthcoming sections of this review we highlight

different plasma based functionalization of graphene and graphene oxide. We also

present the enhanced properties achieved by precise tailoring of these materials.

Attention focuses on functionalization using plasmas of nitrogen, oxygen, hydrogen

and argon.

IV.   Nitrogen functionalization

Theoretical studies have revealed that doping graphene with substitutional

impurities can significantly alter its electronic properties.[57–60] Due to its comparable

atomic radii and five valence electrons, nitrogen has been considered as the appropriate

element for such doping. Additionally, with nitrogen doping it was determined that the

density of states near the Fermi level gets suppressed and the Fermi level shifts above

the Dirac point creating a band gap between its conduction and valence bands. Thus

nitrogen doped graphene manifests semiconducting behaviour. Nitrogen can occupy

different positions on the graphene lattice. In particular, depending upon its bonding

configuration, nitrogen can distort the π electron cloud of graphene and can also

change the hybridization state from sp^2 to sp^3.[61] In the case of GO, changes in oxygen

functionalities on the graphene sheet with nitrogen doping have also been reported.

Thus nitrogen doping extends the application of graphene to semiconductor devices [62],

sensors [63], batteries [64], ultracapacitors [65] and as catalyst in oxygen reduction reactions
[66].

The effect of N_2 plasma functionalization of graphene and highly oriented

pyrolytic graphite (HOPG) was studied by Bertóti *et al.*[67] A constant RF power of

100W at 13.56 MHz was applied on the biased sample. The maximum penetration

depth of the N_2 achieved was 15 Å at 200V bias. The N_2^+ ions could only penetrate the

first 2–4 monolayers of graphene like surfaces and also for HOPG. Ions initiated by lower bias voltage were unable to generate defects and could create covalent bonds with pre-existing defect sites. With the increase in bias voltage the nitrogen content of both the samples were determined to be the same. Indicating the creation of large number of defect sites even in highly crystalline HOPG. Thus plasmas accelerated at sufficient bias voltage can modify the surface of graphene as well as graphite. (refer to Figure 3) Lin *et al.* reported the evolution of graphene from *p*-type to *n*-type by means of gas phase doping using ammonia plasma.[68] Ammonia plasma with flux of 3×10^4 cm^{-2} was applied to the graphene substrate for a range of time intervals on Ni substrate. The nitrogen functionalities (N, NH, NH_2) were determined to form stable covalent bonds even at elevated temperatures. Lin *et al.*[68] concluded that Raman spectra could provide a means for calculating the doping level in graphene. The doping level estimated by the changes in I_{2D}/I_G intensity ratios was determined to be consistent with the electrostatic gating of graphene on silicon substrate. Figure 4 and Figure 5 shows variation in Fermi level and Dirac point with the evolution of G peak in the Raman Spectra. Kato *et al.*[69] used room temperature ammonia plasma to selectively dope the edges of graphene. They used a parameter controlled grid assisted diffusion plasma reactor, which can trigger plasmas with low electron temperature. A rf (13.56 MHz) power source of 20 W was used for this plasma treatment. They confirmed the edge doping by Raman mapping measurements. Reducing entities were determined to favour graphene edges for doping. On increasing the plasma power to 45W there was a substantial decrease in the conductivity of graphene. This reduction in carrier mobility was attributed to increased carrier scattering caused by the rise in defect density in the plane of graphene. There was a difference of 60V of Dirac point for these samples.

These results established a controlled room temperature technique for functionalizing

graphene. Along with electronic properties, surface energy can also be changed using plasma treatment. Baraket et $al.$ [70] reported a change of 12 mJ/m^2 after treatment with ammonia plasma. Nitrogen containing ligands reduced the water contact angle from 98° to 52°, modifying the graphene surface from hydrophobic to hydrophilic. Thus, amine functionalised graphene were determined to be biologically active for DNA detection.

The evolution of n-type behaviour of graphene due to nitrogen incorporation may be due to the increase in concentration of Stone-Wales defect in the graphitic lattice. These defect sites act as electron donor impurity. Zeng et $al.$ [71] deduced that with the increase in rf power the probability of formation of Stone-Wales defect sites increases, thus increasing the electron concentration. Kelvin-probe microscopy was used to examine the work function of graphene treated with different plasmas powers. They determined that the work function of graphene changed from 4.91 eV to 4.37 eV with the increase in plasma power, indicating a change in behaviour form p-type to n-type. They also determined that the Fermi velocity (v_F) of electrons is much lower for the plasma treated graphene in comparison to defect free graphene. The drop in v_F has been related to the increase in disorder after plasma treatment.[72] The reactive species in plasma can not only dope but can also dissociate different functional groups on the lattice. By controlling the substrate temperature and the reaction gases monolayer graphene can be achieved form multilayered graphene structures. Hazra et $al.$[73] achieved monolayer graphene after plasma treatment at substrate temperature ∼400 °C using a gas mixture of N_2 and H_2. Bulk quantities of nitrogen (200 mg) doped graphene nano platelets were synthesized by Jafri et $al.$[74] They used a radio frequency (R.F) magnetron sputtering system working at a frequency of 13.56 MHz and 130 W plasma

power with a chamber pressure of 0.1 mbar. Nitrogen doping created pyrrolic nitrogen defects, which acted as good anchoring sites to attach platinum (Pt) nanoparticles. The disorder also increased the binding energy between the graphene and platinum catalyst. This resulted in improved performance in oxygen reduction reaction (ORR) with respect to graphene/Pt electrodes. Enhanced catalytic property with nitrogen doping, was also reported by Ding *et al.*[75] They synthesized a core shell structure, with platinum nanocrystals encapsulated with graphene as shown in Figure 6. They observed that air plasma treated samples showed the highest percentage of nitrogen doping. An exposure of 5 minutes exhibited the best electrochemical catalytic activity. Thus, the presence of oxygen in the plasma aided the enhanced nitrogen doping. Nitrogen dopants created new activation sites influencing the spin density of the neighbouring carbon atoms. Increased catalytic activity was attributed to the enhanced mobility of the electrons between the graphene and the catalyst. The increase in binding energy between graphene and metal nanoparticles can improve the '*spillover effect*' related to dissociative chemisorption of hydrogen molecule. [76] A uniform dispersion of Pd nanoparticles on graphene was achieved by Parambhath *et al.* [77] with nitrogen plasma treatment. This excellent dispersion is ascribed to the charge transfer between modified electronic structure of graphene and the metallic *d* orbitals. Nitrogen atoms also assist in migration of hydrogen molecules from nanoparticle sites to the adsorbate surface. Raising the hydrogen storage capacity by 272% at 25 °C and 2 MPa pressure. As reported by Shao *et al* [78] a 20 min exposure to nitrogen plasma, manifested higher electrocatalytic activity toward oxygen reduction and H_2O_2 reduction than graphene. From the electrochemical studies they determined that, over potential for the reduction of H_2O_2 was greatly reduced for N-graphene. Figure 7 shows the CV and choronoamperometric response of graphene and N-graphene for

H$_2$O$_2$ reduction. After plasma treatment the oxygen functionalities were determined to

have increased along with the degree of disorder in the graphene lattice. Wang *et al.*[79] also reported the increase in oxygen functionalities after nitrogen plasma treatment. Along with a 27.5 atomic % increase in oxygen content, there was also a decrease in *sp^3* carbon signature in their X-ray photoelectron spectroscopy (XPS) results. For nitrogen-doped graphene the carbon atoms bonded to the nitrogen functional groups possess significantly higher positive charges to negate the strong electron affinity of nitrogen atoms.[80] The increased density of positive charges facilitates the adsorption of molecular oxygen and other reactive species henceforth accelerating the ORR. The enhanced activity of N doped graphene toward H$_2$O$_2$ electrocatalysis, makes it a promising candidate for glucose biosensing.[79] The photocatalytic activity of nitrogen doped monolayer graphene has been reported by Sim *et al.* [81] A 10 Watt Rf (13.56 MHz) power source was used to generate plasma with a maximum exposure time of 16 seconds. The exchange current density (*J$_0$*) for nitrogen doped graphene electrode was determined to be 2.8 times that of bare graphene electrodes indicating a much faster charge transfer between electrodes and electrolyte. It was also observed that a monolayer of graphene with nitrogen moieties could act as an active charge transport layer suppressing the oxidation of the Si photocathodes. Figure 8 shows the enhanced electrocatalytic activity of N-doped graphene as reported by Wang *et al.*[79] and Sim *et al.* [81] Moon *et al.* [82] synthesized blue luminescent graphene quantum sheets by direct nitrogen plasma treatment of CVD graphene on Cu (refer to Figure 9). It is evident from their XPS studies, that the quantum sheets were doped with nitrogen (~2.7%). The N-doped graphene quantum sheets with average size of 4.84 nm could readily be dispersed in organic solvents, making it possible to transfer graphene to any arbitrary shaped photocathode. In a similar work by Sim *et al.* [83] it was suggested that, these

nitrogen doped graphene quantum sheets act as a catalyst for photocataytic hydrogen

evolution on Si nanowire photocathodes. Here the time of plasma exposure being 12 seconds only. The N-doped graphene quantum sheet electrodes exhibited a photon to electron conversion efficiency of 2.29%, higher than any other carbon-based photoelectrochemical hydrogen evolution reaction catalysts. Figure 10 shows the transferred graphene quantum sheets on Si photocathodes along with its domain size.

Jeong et al. [84] developed ultra-capacitors based on plasma processed graphene, manifesting capacitances 4 times higher than pristine graphene based analogues. Using synchrotron based scanning photoemission microscopy they were able to spatially map the different nitrogen configurations at basal planes and at the edges of graphene. Their findings include the increase of pyrrole like nitrogen defects with the increase in plasma exposure along with the decrease in graphitic nitrogen content. Their density functional theory (DFT) calculations were consistent with these experimental findings. Thus the configuration of nitrogen functionalities influences the electrochemical characteristics of graphene.

In most of the studies mentioned above, nitrogen doping was achieved by post synthesis plasma treatments of graphene. Thermally[74] and chemically[78] exfoliated graphene upon nitrogen plasma treatment at elevated temperatures showed a tendency to re-aggregate, impeding its efficiency as battery anodes and supercapacitor electrodes. Kumar et al. [85] addressed this problem by performing simultaneous reduction and nitrogen doping of graphene at room temperature. The reduction was achieved by introducing bulk quantities of graphene oxide to downstream microwave plasma with gas mixture of H_2 and NH_3 (50 sccm each) working at 500W power. The as synthesized samples showed high degree of exfoliation and lower onset potential for oxygen reduction reaction. Among the several doping strategies reported so far each

technique favours specific nitrogen configurations. Lin *et al.*[86] perceived that by

selecting the reactive species it was possible to control the bonding configuration of nitrogen in graphene. They heated the substrate to 850 °C to negate the effect of adsorbates. At this substrate temperature a 10 min exposure to low energy ion beam upshifted the Fermi level by 0.4 eV. Supported by their XPS results, this *n*-type doping was attributed to graphitic nitrogen species. They also determined that the formation of pyridinic nitrogen was initiated after exposure to thermally excited neutral nitrogen. Their results inferred that even low energy ions can substitute carbon atoms in graphitic lattice but neutrals can only fill in pre-existing defects.

There has been a growing interest in applications of graphene in dye-sensitized solar cells (DSSC). [87–89] Graphene is a candidate to replace Pt as counter electrode (CE) for DSSC. Pt shows excellent catalytic activity towards reduction of I_3^- and also posse's high electrical conductivity. Nevertheless, Pt counter electrodes restrict the efficiency of bifacial DSSCs due to it metallic reflectivity.[90] Thus graphene can be a suitable candidate for Pt free bifacial DSSC. Nitrogen doped graphene has already been shown to have better electrocatalytic activity than its pristine counterpart. Yang *et al.*[90] synthesized nitrogen doped graphene using a DC plasma source and used them as counter electrodes. The DSSCs showed an energy conversion efficiency (η) of 3.12% with a treatment time of just 40 seconds. Due to higher transparency the N-doped graphene film CEs exhibited much higher η_{rear}/η_{front} compared to that of Pt as CEs. Graphene CEs also showed superior stability to corrosion with respect to Pt electrodes in the electrolyte. A comparison between the photovoltaic performance of DSSCs with nitrogen doped graphene and platinum counter electrodes is presented in Table 1.

Most of the plasma treatment techniques mentioned above needed low-pressure environment, requiring sophisticated vacuum chambers and pumping systems.

Atmospheric pressure plasma overcomes the drawback of vacuum operation.[91] Lee *et*

al. [92] successfully implemented this technique to dope graphene. An exposure of 20s changed the surface property from hydrophobic to hydrophilic. This change was attributed to the increase in surface functional groups. They were able to achieve a doping level similar to that reported by Lin *et al.*[68] The schematics of the plasma jet and changes in surface contact angle is shown in Figure 11. According to time dependent perturbation theory and the linear dispersion of graphene close to the Dirac point, the level doping can be estimated from the shift of G band ($\Delta\omega_G$) using the following relation.

$$\hbar\Delta\boldsymbol{\omega_G} = \hbar\boldsymbol{\omega_G} - \hbar\boldsymbol{\omega_G^0} = \boldsymbol{\lambda}\left\{|\mathbf{E_F}| + \frac{\hbar\boldsymbol{\omega_G}}{4}\mathbf{ln}\left|\frac{2|\mathbf{E_F}| - \hbar\boldsymbol{\omega_G}}{2|\mathbf{E_F}| + \hbar\boldsymbol{\omega_G}}\right|\right\} \tag{1}$$

$$\text{Where,} \qquad \boldsymbol{\lambda} = \frac{\mathbf{A_{UC}D^2}}{2\boldsymbol{\pi}\hbar\boldsymbol{\omega_G}\mathbf{Mv_F^2}} \tag{2}$$

Here ω_G^0 is the ω_G for undoped sample, E_F is the Fermi level, A_{UC} is the area of the graphene unit cell, v_F the Fermi velocity, D is the electron-phonon coupling of the Γ point phonon having E_{2g} symmetry and M is the atomic mass of carbon.

The large-scale industrial applicability of APPJ was acknowledged by Liu *et al.*[93] They mentioned that surface treatments using APPJ could be four times more effective than other conventional techniques, saving both energy and time. They investigated the effect of APPJ treatment on the DSSC performance. They achieved power conversion efficiency of 5.19% with APPJ treated reduced graphene oxide counter electrodes under illumination of 100 mW cm^{-2}. The estimated power consumption per unit area was 1.1 kJ/cm^2 with a possibility of further reduction. Maximum photon to current conversion efficiency corresponded to 11 seconds treatment, markedly reducing the

processing time. Table 2. Lists the photovoltaic parameters of DSSCs with Pt and

different graphene oxide counter electrodes.

V.   Oxygen Plasma treatment

The prospect of graphene-based nano devices relies on tuning the band gap of graphene. A number of approaches have been pursued to open the band gap of graphene. Chemical doping is the most widely used technique.[17] By customizing the morphology of graphene to nanoribbon [94] and nanodots [30], quantum confinement induced band gap can be achieved. Edges of graphene (zig-zag or armchair) also affect its band gap. Graphene treated with oxygen plasma show enhanced *p*-type behaviour. Shift of Dirac point to positive gate bias voltage confirms the role of oxygen as *p*-type dopant. This evolution of semiconducting behaviour is attributed to the hole doping by O_2 plasma. At 50% O_2 doping the calculated electronic and optical band gap are 3.6 eV and 2 eV respectively.[95] Oxygen plasma introduces epoxy (C−O−C) and carboxyl (C−OH) at the basal plane and edges of graphene, epoxy group being energetically most favourable. DFT calculations on epoxy and hydroxyl modified graphene reveal the transition from semimetal to semiconductor. The presence of these functional groups leads to strong photoluminescence in oxidised graphene. Whereas this effect could not be observed in multilayered graphene structure. Surprisingly the electric transport properties of plasma treated bilayer graphene have considerable resemblance with pristine graphene.[96] Kim *et al.*[97] reported an exponential decrease in the conductance and transconductance for multilayer graphene with oxygen plasma treatment. Reduced mobility was attributed to the 2-D percolative conduction and scattering of the charge careers at the plasma induced defect sites. Detailed Raman spectroscopic studies by Kim *et al.*[98] revealed that the average crystalline size of

graphene decreases with plasma treatment. This effect can be incorporated in the percolation theory to describe the changes in conductance. Characteristic hole doping and shift of Dirac point towards positive gate bias can drive the application of graphene in optoelectronic and sensor applications. Hwang et al. [99] fabricated organic light emitting diodes using multilayered graphene as anode. With oxygen plasma treatment on graphene a significant increase in the injection property was observed, lowering the operating voltage and doubled the power efficiency (14.5 lm/W to 24.1 lm/W).

Surface properties of graphene have been reported to change substantially after oxygen plasma treatment. Plasma treated graphene field effect transistor (FET) was fabricated by Liang et al.[100] The oxygen plasma treatment was determined to enhance the adhesion of graphene with the substrate, but the hole mobility was reduced three times in comparison to graphene FET. The increase in adhesion was attributed to the creation of dangling bonds due to plasma treatment, which in turn acted as surface charge traps. This results were consistent with the findings of Shin et al.[101] They determined that the defects created due to plasma treatment changed graphene form hydrophobic to hydrophilic. Using Raman spectroscopy and water contact angle measurements they were able to correlate degree of disorder with wettability. The surface energy of graphene increased with increase in the level of defects, leading to hydrophilic nature. (Figure 12) By optimising the plasma power and exposure time the wettability of graphene can be improved. Xie et al. [102] applied hexane and oxygen plasma on opposite sides of graphene to instigate asymmetric surface properties. Hexane plasma increased the surface hydrophobicity while oxygen plasma treated surface became highly hydrophilic. Thus the opposite surfaces showed markedly

different electrochemical response. The asymmetric surface properties of graphene

make it possible to fabricate graphene actuators.

For graphene grown via CVD, abundant amount of surface defects are introduced during transfer processes.[103] Polymer residues after fabrication processes affect the electrical and thermal properties of graphene. Plasma treatment can also be used as post process cleaning step for CVD grown graphene.[104] Cleaned graphene showed enhanced conductivity and charge career mobility as shown in Figure 13. Oxygen plasma can induce strong photoluminescence (PL) in pristine graphene. This phenomenon was absent for bilayer and multilayered graphene. C−O bond formation was determined to be the reason for PL rather than quantum confinement effect at the nanometre size sp^2 domains of graphene. Oxygen plasma etches graphite, layer by layer. For graphitic structure the top most layers get oxidised while the bottom layer remains pristine. Thus optical emission form the top layer gets quenched by the pristine bottom layer. Choi et al.[105] reported the terahertz and optical properties of oxygen plasma treated graphene. Raman spectra revealed a blue shift in G band of graphene with plasma treatment accounting for the metal to insulator transition. Thus oxidation results in decrease of free carrier density. These Raman results were consistent with the visible and ultraviolet transmission spectra with similar blue shift in the excitonic absorption peak. After plasma oxidation, graphene showed enhanced transmittance in both the UV and visible region with almost 100% transmission in the 1.5–5.5 eV range. The plasma-generated disorders increased the optical sheet resistance of graphene by 10 times as determined by their terahertz time-domain spectroscopy results. Thus they were able to synthesise highly transparent graphene sheets with elevated sheet resistance, which can find applications in various optoelectronic devices.

High thermal conductivity of graphene accounts for its poor thermoelectric

property. The thermoelectric performance of a material can be measured in terms of a

dimensionless parameter called thermoelectric figure of merit (*ZT*). Where *ZT* is

defined as:

$$ZT = \frac{\sigma\, S^2 T}{\kappa} \qquad (3)$$

Here σ is the electrical conductivity, *S* is the Seebeck coefficient or thermo electric

power, $\kappa = (\kappa_e + \kappa_p)$ is thermal conductivity inclusive of electron and phonon

contributions and *T* is the temperature in Kelvin. The strong energy dependence of the

density of states for graphene and the possibility to achieve high power factor ($\sigma\, S^2$)

makes graphene a probable candidate for recycling heat energy.[106] Due to the

semimetallic behaviour the maximum value of *S* has been calculated to be less than

100 µV/K.[107] The experimentally derived maximum value achieved is 80 µV/K. [108]

With the introduction of defects in graphene, values of *S* and *ZT* can be increased

further.[109] Xiao *et al.* [110] reported maximum thermopower of 700 µV/K at 575 K with

oxygen plasma treatment on few layer graphene. Though the electrical conductivity of

the sample was determined to decrease from 5×10^4 S/m to 10^4 S/m, the increased

thermopower resulted in a significant increase of power factor. The enhanced

thermopower was attributed to structural disorder after plasma treatment and oxygen

functionalities had no effect on the increase. Figure 14 shows variation in the

temperature dependent thermopower and conductivity with plasma treatment.

Transmission electron microscope (TEM) images reveal the loss in crystallinity of

graphene with plasma treatment. Zhao *et al.* [111] studied the variation of thermal

conductivity with lattice defects in graphene. They performed molecular dynamics

(MD) simulation and correlated with non-contact optothermal Raman measurements.

Oxygen plasma treatment was found to decrease the thermal conductivity of graphene

significantly ($\sim$83%) even at extremely low defect concentrations ($\sim$0.1%). Formation

of carbonyl pair defects was determined to be the main reason behind this drop in

conductivity. Other defects such as hydroxyl groups, epoxy groups and vacancies

hardly had any influence. They proposed that a junction between selectively

functionalised graphene and pristine graphene could act as a thermal rectifier with

rectification ratio of $\sim$46%.

Plasma treatment has been determined to reduce the contact resistance at

graphene-metal interface.[112] Plasma generated defects and dangling bonds result in the

cohesive orbital overlap between Sp^2 carbon and metal d orbital enhancing the carrier

transmission. Morphology of the metal graphene contact also controls the contact

resistance. Due to the presence of stable π bonds on the graphene surface larger

coupling length is expected. While for the end contact junction formation of

covalent/ionic bonds reduce the coupling length. Figure 15 illustrates the morphology

changes along with the variation in contact resistance with oxygen plasma treatment.

Oxygen plasma has been used to fabricate transparent graphene electrodes of flexible

plastic substrates.[113] The patterned graphene electrode exhibited a high conductivity of

80 S cm^{-1} and transparency of 76%. Recently Surwade et $al.$ showed the application of

nanoporous graphene as membrane for water desalination.[114] Oxygen plasma was used

to create nanopores of precise dimensions on the graphene lattice. The synthesised

nanopores showed exceptional selectivity to water molecules with respect to dissolved

K^+, Na^+, Li^+, and Cl^-. They also tried electrons of varying energies (250 V to 20 kV)

and gallium ions with energy of 30 kV. Defects created by these entities were similar

to those created by oxygen plasma, but these membranes showed negligible water

transport with respect to the plasma treated one. Proving oxygen plasma to be the ideal

21

candidate for this purpose. The nanopores showed an extremely high water flux of

three molecules per picosecond when the average nanopore density was 1/100 nm^2 and exceeded their theoretical estimated values by an order of magnitude. These membranes showed poor water flux (200 molecules/microsecond) when applied with osmotic pressure gradient. Thus industrial applicability of nanoporous graphene still remains a challenge.

Oxygen plasma can also enhance the molecular properties of graphene. In a report by Mao *et al.* [115] it was determined that graphene treated with mild oxygen plasma showed pronounced Raman peaks of adsorbed Rhodamine B molecules. Most intense Raman peak corresponded to O_2 plasma (5 Watt) treatment for just 10 secs. Due to the difference in electronegativity between carbon and oxygen, the increased oxygen functionalities created strong local dipole moments. This resulted in an intense local electric field on the adsorbed molecules. Another reason for the enhanced Raman signal may be the *p*-doping of graphene. This downshift of the graphene Fermi level reduces the energy gap between the lowest unoccupied molecular orbital (LUMO) of adsorbed molecules and the Fermi level. With the advantages of plasma, the oxygenated graphene can provide a propitious stage for molecular sensing.

VI.   Hydrogenation

Elias *et al.* [116] reported that graphene in spite of being chemically inert, can react with atomic hydrogen. The reaction can bring substantial changes in its electronic and structural properties. They determined that hydrogenation opened up a band gap transforming graphene from highly conductive semimetal to insulator. Band gap opening was attributed to the change in hybridization of carbon atoms from sp^2 into sp^3,

removing the conducting π bands. Hydrogenated graphene retained the crystalinity and

hexagonal structure of the lattice. Notably, the periodicity was markedly reduced. The neutrality point shifted towards positive values of gate voltage indicating *p* type doping. Also the charge carriers exhibited 2-D variable range hopping. Nevertheless, by annealing they were able to restore the properties of pristine graphene. Indicating hydrogenation being a reversible process. Similar changes have been observed by Wojtaszek *et al.*[117]. They carried out hydrogenation in a reactive ion etching system with Ar-Hydrogen gas mixture. They were first to use this technique to carry out hydrogenation of graphene. By controlling the applied bias voltage at the graphene electrode, hydrogenation can be carried out without the sputtering of the carbon atoms form the graphene lattice. Defects induced by hydrogen plasma were determined to reduce the electron transfer barrier at the interface of graphene and organic semiconductor. Interfacial dipoles created between graphene and $F_{16}CuPc$ (hexadecafluorophthalocya-nine) was hugely reduced by treating graphene with hydrogen plasma.[118] This indicates that tuning the defect density in graphene by hydrogen plasma is a suitable for controlling electronic transport characteristics and performance of organic electronic devices with graphene electrodes. Figure 16 shows the band alignment between graphene and $F_{16}CuPc$ with plasma treatment. Eren *et al.*[119] investigated the optical response of graphene to hydrogen plasma treatment using ellipsometry measurements. They observed changes in electronic and Raman spectra. Hydrogenation could not affect the optical properties of graphene. With low energy hydrogen plasma, graphene was determined to retain its conductivity with $T^{1/3}$ dependence of the electrical resistivity. Whereas, the high-energy hydrogen ions sputtered carbon atoms, causing significant defects in the graphene lattice. Elipsometric measurements revealed that hydrogenated graphene did not show any

absorbance at $\lambda \leq 500$ nm. Absorbance (E) was determined to be constant below the

Van Hove singularity, a characteristic of conducting 2-D materials. After chemical sputtering, graphene showed absorbance at $\lambda \leq 500$ nm. Thus plasma-induced defect brings about changes in optical transport of graphene. Xie et al. [120] were able to selective etch graphene along its edges. They established that hydrogenation and reverse hydrogenation processes could be balanced at milder temperature (300 °C) without introducing any defects at the basal plane. They performed the same plasma treatment at room temperature and at elevated temperature (500 °C). Both cases showed formation of defects in the basal plane. The formation of stable C−H bonds along the edges lead to the cleavage of adjacent C−C bonds. Using this selective etching along the edges they were able to narrow down 14 nm wide graphene nanoribbon (GNR) to less than 5 nm. This trimmed GNRs exhibited semiconducting characteristics with high on/off ratios (~1000) at room temperature. Figure 17 shows the changes in gate source voltage with plasma etching of graphene. Yang et al. [121] stated that the etching strongly depends on the crystallographic orientation of graphene. Etching occurred at a faster rate along the $[2\bar{1}\bar{1}0]$ and slowest along $[10\bar{1}0]$ direction. They also stated that the H radicals attacked the carbon atoms at the edges. Forming stable C−H bonds resulting in breakage of C−C bonds. Figure 18 is a schematic representation of the fabrication of GNR arrays. In the report by Luo et al. [122] it was mentioned that both hydrogenation and dehydrogenation had a significant dependence on the number of layers. Hydrogenation barrier for graphene is higher than that of graphitic surface. By virtue of its lower hydrogenation barrier multi-layered graphene get hydrogenated much faster than single layered graphene. Thus by controlling the plasma power and process time tailored structures of graphene can be achieved along

with precise hydrogen coverage. This technique for graphene etching can be ideal

suited to precisely tailor graphene without degrading its quality.

In plane ballistic charge transport characteristics and high mechanical strength makes graphene an ideal candidate for electron microscope (EM) support stages. Graphene being hydrophobic in nature renders it incompatible for biological applications. Due to decreased conductivity resulting in accumulation of surface charge makes its oxide counterpart less ideal as EM support stage. Russo and Passmore [123] determined that graphene treated with low energy hydrogen plasma behaves as hydrophilic. According to them the hydrogenation occurs via the reaction:

$$sp^2\,C + H \;\leftrightarrow\; sp^3\,CH \qquad\qquad (4)$$

The water contact angle was found to decrease exponentially from a value of $91 \pm 0.5°$ to a saturation value of $66 \pm 1.3°$ corresponding to a drop of 0.19 ± 0.02 eV/nm^2 in graphene water interfacial energy. Even with hydrogenation the graphene lattice remained conserved. The adsorption of protein molecules on graphene grid was found to increase substantially after hydrogenation along with improved quality of cryo-EM images as shown in Figure 19. Thus the hydrogen plasma treated graphene can provide a stable platform for detection and characterization of biological entities. Felten *et al.* [124] reported a detailed study on the influence of different plasma parameters that effect and control the hydrogenation of graphene. They were able to correlate between structural modifications with the energy distribution of the hydrogen ions with Raman spectroscopy and Mass spectroscopy. Energy of the ionic species present in Hydrogen plasma (H^+, H_2^+, H_3^+) reaching the graphene substrate strongly depend on the sample position, chamber pressure and plasma power. The maximum value of ionic energy

they could achieve is 45 eV. This is much higher than the theoretically calculated

proton transfer barriers of graphene.[125] Thus with precise control over the plasma energy and knowledge of the ionic species graphene layers can be cleaned, functionalized or even etched away layer by layer.

VII. Ar Plasma

Some of the properties of graphene such as high aspect ratio, presence of abundant edges along with its excellent conductivity make it an ideal candidate for use in fuel cell [66,126], Li-ion batteries [65,127,128], supercapacitor [90,91] and field emission sources [131,132].

Irradiating graphene with low energy (1 KeV) Ar^+ ions was determined to bring changes in its surface morphology and electronic structure.[133] The irradiation increased the sp^3 domains and also changed the density of states near the Fermi level. Qi *et al.* [134] found enhanced field emission of graphene with Ar plasma treatment, synthesised via radio frequency PECVD on Si (100) substrates. The plasma treatment on the as grown few layer graphene Sheets (FLGs) was carried out with 10 sccm Ar flow. The operating conditions were temperature $\approx$ 800 °C , pressure $\approx$ 150 Pa and radio frequency power $\approx$ 150 W with etching times of 1 min, 3 min and 5 min. The turn-on electric fields after 1 min, 3 min and 5 min were determined to be 2.87 Vμm^{-1}, 2.23 Vμm^{-1} and 2.63 Vμm^{-1}, respectively whereas for the as-synthesized sample it was 3.91 μm^{-1}. After 3 min treatment the maximum emission current density at a field of 4.4V μm^{-1} increased significantly from 33 μAcm^{-2} for pristine sample to 1330 μAcm^{-2}. Variation in the field emission of few layer graphene with plasma exposure time is shown in Figure 20. The enhanced field emission was attributed to the etching of the folded edges to sharp and upright edges by Ar plasma. With prolonged exposure the sharp edges become blunt decreasing the electric field strength at the edges. (Refer to

Figure 21) Liu *et al.* [135] reported improved field emission form graphene paper, which

was synthesized by annealing graphene oxide at 500 °C. They carried out the plasma treatment in a dc magnetron sputtering system with 2 Pa background pressure and 150 W power. They determined that Ar plasma created ridges on the surface of graphene paper. Due to increased field concentration, these formed ridges could emit electron at lower field. According to their report after 3 min Ar plasma treatment, turn-on field and threshold field of the GP were reduced from 2.3 V/μm to 1.6 V/ μm and 4.4 V/ μm to 3.0 V/ μm respectively. Ar plasma annihilated the structural stacking and caused the formation of sharp surface features. These features changed the characteristics of graphene paper from hydrophilic to hydrophobic. These results were in accordance with the findings of Qi *et al.* [134]

Due to the broadband transparency and ultrawideband tunability graphene has attracted enormous interest in the field of photonic and optoelectronic applications.[15,136] The photoresponse of graphene have been widely studied in recent years.[137–139] The inferior absorption (2.3%) and short recombination lifetimes (~1.5 ps) of the photogenerated charge carriers the sensitivity of graphene photodetector is low.[140] Thiyagarajan *et al.* [141] observed a significant increase in visible light photoresponse with plasma irradiation of FLG. They used an atmospheric pressure plasma reactor working at 1 Torr pressure with 60 sccm Ar flow. Plasma exposure was for 5 mins. Visible light (535nm) photoresponsivity increased to 0.47 AW^{-1} from 10 mA/m^{-1} after plasma treatment. Plasma induced defects and oxygen functionalities resulting in formation of midgap states were responsible for this increase. The photocurrent values at 535 nm, 405 nm and 365 nm were determined to be 19.16 μA, 13.31μA and 7.67 μA respectively. Figure 22 demonstrates the enhanced photoresponce of FLG with the introduction of mid band states. Thiyagarajan *et al.* [142]

reported that the gate tunable photoresponse of this defective graphene in the UV and visible region. On exposure to visible wavelengths (405 nm and 535 nm) V_{Dirac} shifted to 45 V while for UV (365 nm) exposure the Dirac point shifted to 22 V. Thus plasma exposure resulted in *p*-doping and with UV exposure photoinduced desorption started causing *n*-doping. The induced defects after plasma treatment act as charge separation sites enhancing the photoresponse. Thus by controlling the defect density of graphene, its photoresponse can be tuned. Narayanan *et al.* [143] showed that the plasma generated defect could substantially increase the electrical capacitance of few layer graphene for electrochemical energy storage. The increase was not consistent with the increase in plasma power. (refer to Table 3) Capacitance doubled for 20 W plasma power with respect to the pristine sample (1.9 µFcm^{-2} to 4.7 µFcm^{-2}) and dropped when the plasma power was increased beyond 35 W. This may be due to increased disorder in the lattice or etching of the graphene structure. They also proposed a new length scale L_d and correlated it to the distance between electrically active defect sites, which contribute to capacitance. L_d is smaller than the conventional Tuinstra−Koenig correlation length (structural length scale determined through Raman spectroscopy). Where $L_d = 1/(n_{2D,0})^{1/2}$. Thus distinguishing between structural and electrical length scales for defective graphene.

VIII.   Summary and Future perspectives

A significant amount of research has been performed on graphene during the last decade. This is driven by the realisation of the immense capabilities possessed by this wonder material. Applications already recognized ranges from ultra-fast and flexible electronics to optoelectronic devices, supercapacitors, water remediation, DNA

attachment, photocatalysis, oxygen reduction reaction catalysts and many more. To realize these pathways functionalization of graphene and its oxide played a crucial role. Many techniques of functionalization have been applied to extend the potential applications of graphene. [142]

In the present review we discuss plasma functionalization as a potent alternative to conventional techniques. Plasma functionalization is advantageous in terms of controllability and selectivity associated with it. The ionic species present in plasma can tune electronic and optical properties of graphene and can even control the surface hydrophobicity. Wet chemical functionalization involving precursors and by-products fails in achieving localized effects in graphene and GO. With plasma functionalization we can precisely tailor graphene properties by inducing localised changes. Advantages of this technique include time and cost effectiveness. This process being clean and reliable opens up future pathways for large-scale industrial implementation. Table 4 presents a summary of this article. Here we mentioned the plasma parameters used for functionalization and thus the enhanced properties achieved. However, most of the plasma processes involve low-pressure vacuum based systems. APPJ can be a promising candidate for various plasma based functionalization applications. In APPJ plasma is not confined within the dimensions of the electrodes. This low temperature and atmospheric pressure process can be used for large-scale roll-to-roll functionalization of graphene and GO.

IX.   Acknowledgments

References

[1] K.S. Novoselov, A.K. Geim, S. V Morozov, D. Jiang, Y. Zhang, S. V Dubonos, I. V Grigorieva, and A.A. Firsov, Science **306**, 666 (2004).

[2] A.A. Balandin, S. Ghosh, W. Bao, I. Calizo, D. Teweldebrhan, F. Miao, and C.N. Lau, Nano Lett. **8**, 902 (2008).

[3] A.S. Mayorov, R. V Gorbachev, S. V Morozov, L. Britnell, R. Jalil, L.A. Ponomarenko, P. Blake, K.S. Novoselov, K. Watanabe, T. Taniguchi, and A.K. Geim, Nano Lett. **11**, 2396 (2011).

[4] S. Morozov, K. Novoselov, M. Katsnelson, F. Schedin, D. Elias, J. Jaszczak, and A. Geim, Phys. Rev. Lett. **100**, 016602 (2008).

[5] M.D. Stoller, S. Park, Y. Zhu, J. An, and R.S. Ruoff, Nano Lett. **8**, 3498 (2008).

[6] R.R. Nair, P. Blake, A.N. Grigorenko, K.S. Novoselov, T.J. Booth, T. Stauber, N.M.R. Peres, and A.K. Geim, Science **320**, 1308 (2008).

[7] J. Moser, A. Barreiro, and A. Bachtold, Appl. Phys. Lett. **91**, 163513 (2007).

[8] T. Ando, NPG Asia Mater. **1**, 17 (2009).

[9] K.S. Novoselov, A.K. Geim, S. V Morozov, D. Jiang, M.I. Katsnelson, I. V Grigorieva, S. V Dubonos, and A.A. Firsov, Nature **438**, 197 (2005).

[10] C. Lee, X. Wei, J.W. Kysar, and J. Hone, Science **321**, 385 (2008).

[11] J.S. Bunch, S.S. Verbridge, J.S. Alden, A.M. van der Zande, J.M. Parpia, H.G. Craighead, and P.L. McEuen, Nano Lett. **8**, 2458 (2008).

[12] K.P. Loh, Q. Bao, P.K. Ang, and J. Yang, J. Mater. Chem. **20**, 2277 (2010).

[13] K.S. Novoselov, V.I. Fal'ko, L. Colombo, P.R. Gellert, M.G. Schwab, and K. Kim, Nature **490**, 192 (2012).

[14] R. Raccichini, A. Varzi, S. Passerini, and B. Scrosati, Nat. Mater. **14**, 271 (2015).

[15] F. Bonaccorso, Z. Sun, T. Hasan, and A.C. Ferrari, Nat. Photonics **4**, 611 (2010).

[16] P.T. Yin, S. Shah, M. Chhowalla, and K.-B. Lee, Chem. Rev. **115**, 2483 (2015).

[17] H. Liu, Y. Liu, and D. Zhu, J. Mater. Chem. **21**, 3335 (2011).

[18] T. Kuila, S. Bose, A.K. Mishra, P. Khanra, N.H. Kim, and J.H. Lee, Prog. Mater. Sci. **57**, 1061 (2012).

[19] X. Wang, X. Li, L. Zhang, Y. Yoon, P.K. Weber, H. Wang, J. Guo, and H. Dai, Science **324**, 768 (2009).

[20] G. Giovannetti, P.A. Khomyakov, G. Brocks, V.M. Karpan, J. van den Brink, and P.J. Kelly, Phys. Rev. Lett. **101**, 026803 (2008).

[21] C.E. Malec and D. Davidović, Phys. Rev. B **84**, 033407 (2011).

[22] F. Schedin, A.K. Geim, S. V Morozov, E.W. Hill, P. Blake, M.I. Katsnelson, and K.S. Novoselov, Nat. Mater. **6**, 652 (2007).

[23] Y. Xu, Z. Liu, X. Zhang, Y. Wang, J. Tian, Y. Huang, Y. Ma, X. Zhang, and Y. Chen, Adv. Mater. **21**, 1275 (2009).

[24] W. Chen, S. Chen, D.C. Qi, X.Y. Gao, and A.T.S. Wee, J. Am. Chem. Soc. **129**, 10418 (2007).

[25] D. Li, M.B. Müller, S. Gilje, R.B. Kaner, and G.G. Wallace, Nat. Nanotechnol. **3**, 101 (2008).

[26] S. Stankovich, D.A. Dikin, R.D. Piner, K.A. Kohlhaas, A. Kleinhammes, Y. Jia, Y. Wu, S.T. Nguyen, and R.S. Ruoff, Carbon N. Y. **45**, 1558 (2007).

[27] X. Li, X. Wang, L. Zhang, S. Lee, and H. Dai, Science **319**, 1229 (2008).

[28] D. V Kosynkin, A.L. Higginbotham, A. Sinitskii, J.R. Lomeda, A. Dimiev, B.K. Price, and J.M. Tour, Nature **458**, 872 (2009).

[29] D. Jiang, B.G. Sumpter, and S. Dai, J. Chem. Phys. **126**, 134701 (2007).

[30] L.A. Ponomarenko, F. Schedin, M.I. Katsnelson, R. Yang, E.W. Hill, K.S. Novoselov, and A.K. Geim, Science **320**, 356 (2008).

[31] D. Pan, J. Zhang, Z. Li, and M. Wu, Adv. Mater. **22**, 734 (2010).

[32] Z.H. Ni, T. Yu, Y.H. Lu, Y.Y. Wang, Y.P. Feng, and Z.X. Shen, ACS Nano **3**, 483 (2009).

[33] W.S. Hummers and R.E. Offeman, J. Am. Chem. Soc. **80**, 1339 (1958).

[34] G. Eda, G. Fanchini, and M. Chhowalla, Nat. Nanotechnol. **3**, 270 (2008).

[35] B.C. Brodie, Philos. Trans. R. Soc. London **149**, 249 (1859).

[36] D. Chen, H. Feng, and J. Li, Chem. Rev. **112**, 6027 (2012).

[37] K.P. Loh, Q. Bao, G. Eda, and M. Chhowalla, Nat. Chem. **2**, 1015 (2010).

[38] M. Zhou, Y. Zhai, and S. Dong, Anal. Chem. **81**, 5603 (2009).

[39] O.C. Compton and S.T. Nguyen, Small **6**, 711 (2010).

[40] D. Szabó and S. Schlabach, Inorganics **2**, 468 (2014).

[41] G.S. Selwyn, H.W. Herrmann, J. Park, and I. Henins, Contrib. to Plasma Phys. **41**, 610 (2001).

[42] J. Laimer and H. Störi, Plasma Process. Polym. **4**, 266 (2007).

[43] M. Laroussi, C. Tendero, X. Lu, S. Alla, and W.L. Hynes, Plasma Process. Polym. **3**, 470 (2006).

[44] J.H. Noh, H.K. Baik, I. Noh, J.-C. Park, and I.-S. Lee, Surf. Coatings Technol. **201**, 5097 (2007).

[45] O. V. Penkov, M. Khadem, W.-S. Lim, and D.-E. Kim, J. Coatings Technol. Res. **12**, 225 (2015).

[46] D. Marinov and N.S.J. Braithwaite, Plasma Sources Sci. Technol. **23**, 062005 (2014).

[47] E.T. Thostenson, Z. Ren, and T.-W. Chou, Compos. Sci. Technol. **61**, 1899 (2001).

[48] Q. Zhao, Z. Gan, and Q. Zhuang, Electroanalysis **14**, 1609 (2002).

[49] R.H. Baughman, A.A. Zakhidov, and W.A. de Heer, Science **297**, 787 (2002).

[50] J.N. Coleman, U. Khan, and Y.K. Gun'ko, Adv. Mater. **18**, 689 (2006).

[51] H. Abe, M. Yoneda, and N. Fujiwara, Jpn. J. Appl. Phys. **47**, 1435 (2008).

[52] M. Meyyappan, J. Phys. D. Appl. Phys. **44**, 174002 (2011).

[53] M. Meyyappan, J. Phys. D. Appl. Phys. **42**, 213001 (2009).

[54] E.C. Neyts, J. Vac. Sci. Technol. B Microelectron. Nanom. Struct. **30**, 030803 (2012).

[55] Q. Wang, X. Wang, Z. Chai, and W. Hu, Chem. Soc. Rev. **42**, 8821 (2013).

[56] Z. Bo, Y. Yang, J. Chen, K. Yu, J. Yan, and K. Cen, Nanoscale **5**, 5180 (2013).

[57] F. Cervantes-Sodi, G. Csányi, S. Piscanec, and a. C. Ferrari, Phys. Rev. B - Condens. Matter Mater. Phys. **77**, 1 (2008).

[58] L. Tsetseris, B. Wang, and S.T. Pantelides, Phys. Rev. B **89**, 035411 (2014).

[59] T.B. Martins, R.H. Miwa, A.J.R. da Silva, and A. Fazzio, Phys. Rev. Lett. **98**, 196803 (2007).

[60] M. Calandra and F. Mauri, Phys. Rev. B **76**, 161406 (2007).

[61] D. Wei, Y. Liu, Y. Wang, H. Zhang, L. Huang, and G. Yu, Nano Lett. **9**, 1752 (2009).

[62] B. Guo, Q. Liu, E. Chen, H. Zhu, L. Fang, and J.R. Gong, Nano Lett. **10**, 4975 (2010).

[63] R. Lv, Q. Li, A.R. Botello-Méndez, T. Hayashi, B. Wang, A. Berkdemir, Q. Hao, A.L. Elías, R. Cruz-Silva, H.R. Gutiérrez, Y.A. Kim, H. Muramatsu, J. Zhu, M. Endo, H. Terrones, J.-C. Charlier, M. Pan, and M. Terrones, Sci. Rep. **2**, 586 (2012).

[64] A.L.M. Reddy, A. Srivastava, S.R. Gowda, H. Gullapalli, M. Dubey, and P.M. Ajayan, ACS Nano **4**, 6337 (2010).

[65] Z.-S. Wu, W. Ren, L. Xu, F. Li, and H.-M. Cheng, ACS Nano **5**, 5463 (2011).

[66] L. Qu, Y. Liu, J.-B. Baek, and L. Dai, ACS Nano **4**, 1321 (2010).

[67] I. Bertóti, M. Mohai, and K. László, Carbon N. Y. **84**, 185 (2015).

[68] Y.C. Lin, C.Y. Lin, and P.W. Chiu, Appl. Phys. Lett. **96**, 133110 (2010).

[69] T. Kato, L. Jiao, X. Wang, H. Wang, X. Li, L. Zhang, R. Hatakeyama, and H. Dai, Small **7**, 574 (2011).

[70] M. Baraket, R. Stine, W.K. Lee, J.T. Robinson, C.R. Tamanaha, P.E. Sheehan, and S.G. Walton, Appl. Phys. Lett. **100**, (2012).

[71] J.J. Zeng and Y.J. Lin, Appl. Phys. Lett. **104**, 1 (2014).

[72] L. Tapasztó, G. Dobrik, P. Nemes-Incze, G. Vertesy, P. Lambin, and L.P. Biró, Phys. Rev. B **78**, 233407 (2008).

[73] K.S. Hazra, J. Rafiee, M. a Rafiee, a Mathur, S.S. Roy, J. McLauhglin, N. Koratkar, and D.S. Misra, Nanotechnology **22**, 025704 (2011).

[74] R. Imran Jafri, N. Rajalakshmi, and S. Ramaprabhu, J. Mater. Chem. **20**, 7114 (2010).

[75] D. Ding, Z.-L. Song, Z.-Q. Cheng, W.-N. Liu, X.-K. Nie, X. Bian, Z. Chen, and W.

Tan, J. Mater. Chem. A **2**, 472 (2014).

[76] A.J. Lachawiec, G. Qi, and R.T. Yang, Langmuir **21**, 11418 (2005).

[77] V.B. Parambhath, R. Nagar, and S. Ramaprabhu, Langmuir **28**, 7826 (2012).

[78] Y. Shao, S. Zhang, M.H. Engelhard, G. Li, G. Shao, Y. Wang, J. Liu, I. a. Aksay, and Y. Lin, J. Mater. Chem. **20**, 7491 (2010).

[79] Y. Wang, Y. Shao, D.W. Matson, J. Li, and Y. Lin, ACS Nano **4**, 1790 (2010).

[80] K. Gong, F. Du, Z. Xia, M. Durstock, and L. Dai, Science **323**, 760 (2009).

[81] U. Sim, T.-Y. Yang, J. Moon, J. An, J. Hwang, J.-H. Seo, J. Lee, K.Y. Kim, J. Lee, S. Han, B.H. Hong, and K.T. Nam, Energy Environ. Sci. **6**, 3658 (2013).

[82] J. Moon, J. An, U. Sim, S.P. Cho, J.H. Kang, C. Chung, J.H. Seo, J. Lee, K.T. Nam, and B.H. Hong, Adv. Mater. **26**, 3501 (2014).

[83] U. Sim, J. Moon, J. An, J.H. Kang, S.E. Jerng, J. Moon, S.-P. Cho, B.H. Hong, and K.T. Nam, Energy Environ. Sci. **8**, 1329 (2015).

[84] H.M. Jeong, J.W. Lee, W.H. Shin, Y.J. Choi, H.J. Shin, J.K. Kang, and J.W. Choi, Nano Lett. **11**, 2472 (2011).

[85] N.A. Kumar, H. Nolan, N. McEvoy, E. Rezvani, R.L. Doyle, M.E.G. Lyons, and G.S. Duesberg, J. Mater. Chem. A **1**, 4431 (2013).

[86] Y.P. Lin, Y. Ksari, J. Prakash, L. Giovanelli, J.C. Valmalette, and J.M. Themlin, Carbon N. Y. **73**, 216 (2014).

[87] J.D. Roy-Mayhew, D.J. Bozym, C. Punckt, and I.A. Aksay, ACS Nano **4**, 6203 (2010).

[88] H. Choi, H. Kim, S. Hwang, Y. Han, and M. Jeon, J. Mater. Chem. **21**, 7548 (2011).

[89] Y. Xue, J. Liu, H. Chen, R. Wang, D. Li, J. Qu, and L. Dai, Angew. Chem. Int. Ed. Engl. **51**, 12124 (2012).

[90] W. Yang, X. Xu, Z. Tu, Z. Li, B. You, Y. Li, S.I. Raj, F. Yang, L. Zhang, S. Chen, and A. Wang, Electrochim. Acta **173**, 715 (2015).

[91] A. Schutze, J.Y. Jeong, S.E. Babayan, G.S. Selwyn, and R.F. Hicks, IEEE Trans. Plasma Sci. **26**, 1685 (1998).

[92] B.-J. Lee, S.-C. Cho, and G.-H. Jeong, Curr. Appl. Phys. **15**, 563 (2015).

[93] H.-W. Liu, S. Liang, T.-J. Wu, H. Chang, P.-K. Kao, C.-C. Hsu, J.-Z. Chen, P.-T. Chou, and I. Cheng, ACS Appl. Mater. Interfaces **6**, 15105 (2014).

[94] M. Han, B. Özyilmaz, Y. Zhang, and P. Kim, Phys. Rev. Lett. **98**, 206805 (2007).

[95] A. Nourbakhsh, M. Cantoro, T. Vosch, G. Pourtois, F. Clemente, M.H. van der Veen, J. Hofkens, M.M. Heyns, S. De Gendt, and B.F. Sels, Nanotechnology **21**, 435203 (2010).

[96] A. Nourbakhsh, M. Cantoro, A. V. Klekachev, G. Pourtois, T. Vosch, J. Hofkens, M.H. van der Veen, M.M. Heyns, S. De Gendt, and B.F. Sels, J. Phys. Chem. C **115**, 16619 (2011).

[97] K. Kanghyun, J.P. Hyung, B.C. Woo, J.K. Kook, T.K. Gyu, and S.Y. Wan, Nano

Lett. **8**, 3092 (2008).

[98] D.C. Kim, D.-Y. Jeon, H.-J. Chung, Y. Woo, J.K. Shin, and S. Seo, Nanotechnology **20**, 375703 (2009).

[99] J. Hwang, H. Kyw Choi, J. Moon, T. Yong Kim, J.W. Shin, C. Woong Joo, J.H. Han, D.H. Cho, J. Woo Huh, S.Y. Choi, J.I. Lee, and H. Yong Chu, Appl. Phys. Lett. **100**, 2 (2012).

[100] X. Liang, Z. Fu, and S.Y. Chou, Nano Lett. **7**, 3840 (2007).

[101] Y.J. Shin, Y. Wang, H. Huang, G. Kalon, A.T.S. Wee, Z. Shen, C.S. Bhatia, and H. Yang, Langmuir **26**, 3798 (2010).

[102] X. Xie, L. Qu, C. Zhou, Y. Li, J. Zhu, H. Bai, G. Shi, and L. Dai, ACS Nano **4**, 6050 (2010).

[103] J.W. Suk, W.H. Lee, J. Lee, H. Chou, R.D. Piner, Y. Hao, D. Akinwande, and R.S. Ruoff, Nano Lett. **13**, 1462 (2013).

[104] N. Peltekis, S. Kumar, N. McEvoy, K. Lee, A. Weidlich, and G.S. Duesberg, Carbon N. Y. **50**, 395 (2012).

[105] K. Choi, J. Lim, J.R. Rani, H. Seo Yoon, J. Oh, T. Hong, T. Ha, B. Cheol Park, K. Ik Sim, S. Chan Jun, and J. Hoon Kim, Appl. Phys. Lett. **102**, 2011 (2013).

[106] P. Dollfus, V. Hung Nguyen, and J. Saint-Martin, J. Phys. Condens. Matter **27**, 133204 (2015).

[107] Y. Ouyang and J. Guo, Appl. Phys. Lett. **94**, 263107 (2009).

[108] Y.M. Zuev, W. Chang, and P. Kim, Phys. Rev. Lett. **102**, 1 (2009).

[109] A. a Balandin, Nat. Mater. **10**, 569 (2011).

[110] N. Xiao, X. Dong, L. Song, D. Liu, Y. Tay, S. Wu, L.J. Li, Y. Zhao, T. Yu, H. Zhang, W. Huang, H.H. Hng, P.M. Ajayan, and Q. Yan, ACS Nano **5**, 2749 (2011).

[111] W. Zhao, Y. Wang, Z. Wu, W. Wang, K. Bi, Z. Liang, J. Yang, Y. Chen, Z. Xu, and Z. Ni, Sci. Rep. **5**, 11962 (2015).

[112] D.W. Yue, C.H. Ra, X.C. Liu, D.Y. Lee, and W.J. Yoo, Nanoscale **7**, 825 (2015).

[113] J.H. Kim, E. Ko, J. Hwang, X.-H. Pham, J.H. Lee, S.H. Lee, V.-K. Tran, J.-H. Kim, J.-G. Park, J. Choo, K.N. Han, and G.H. Seong, Langmuir **31**, 2914 (2015).

[114] S.P. Surwade, S.N. Smirnov, I. V. Vlassiouk, R.R. Unocic, G.M. Veith, S. Dai, and S.M. Mahurin, Nat. Nanotechnol. **10**, 459 (2015).

[115] H. Mao, R. Wang, J. Zhong, S. Zhong, and W. Chen, Carbon N. Y. **76**, 212 (2014).

[116] D.C. Elias, R.R. Nair, T.M.G. Mohiuddin, S. V Morozov, P. Blake, M.P. Halsall, a C. Ferrari, D.W. Boukhvalov, M.I. Katsnelson, a K. Geim, and K.S. Novoselov, Science **323**, 610 (2009).

[117] M. Wojtaszek, N. Tombros, A. Caretta, P.H.M. Van Loosdrecht, and B.J. Van Wees, J. Appl. Phys. **110**, 1 (2011).

[118] Q.-D. Yang, W.-D. Dou, C. Wang, H.-W. Mo, M.-F. Lo, M.F. Yuen, T.-W. Ng, W.-J. Zhang, S.-W. Tsang, and C.-S. Lee, Appl. Phys. Lett. **106**, 133502 (2015).

[119] B. Eren, W. Fu, L. Marot, M. Calame, R. Steiner, and E. Meyer, To Be Submitt. **106**, 011904 (2015).

[120] L. Xie, L. Jiao, and H. Dai, J. Am. Chem. Soc. **132**, 14751 (2010).

[121] R. Yang, L. Zhang, Y. Wang, Z. Shi, D. Shi, H. Gao, E. Wang, and G. Zhang, Adv. Mater. **22**, 4014 (2010).

[122] Z. Luo, T. Yu, K.J. Kim, Z. Ni, Y. You, S. Lim, Z. Shen, S. Wang, and J. Lin, ACS Nano **3**, 1781 (2009).

[123] C.J. Russo and L. a Passmore, Nat. Methods **11**, 649 (2014).

[124] a. Felten, D. McManus, C. Rice, L. Nittler, J.-J. Pireaux, and C. Casiraghi, Appl. Phys. Lett. **105**, 183104 (2014).

[125] E. Despiau-Pujo, A. Davydova, G. Cunge, L. Delfour, L. Magaud, and D.B. Graves, J. Appl. Phys. **113**, 114302 (2013).

[126] J. Hou, Y. Shao, M.W. Ellis, R.B. Moore, and B. Yi, Phys. Chem. Chem. Phys. **13**, 15384 (2011).

[127] E. Yoo, J. Kim, E. Hosono, H. Zhou, T. Kudo, and I. Honma, Nano Lett. **8**, 2277 (2008).

[128] P. Lian, X. Zhu, S. Liang, Z. Li, W. Yang, and H. Wang, Electrochim. Acta **55**, 3909 (2010).

[129] Y. Zhu, S. Murali, M.D. Stoller, K.J. Ganesh, W. Cai, P.J. Ferreira, A. Pirkle, R.M. Wallace, K. a Cychosz, M. Thommes, D. Su, E. a Stach, and R.S. Ruoff, Science **332**, 1537 (2011).

[130] Y. Wang, Z. Shi, Y. Huang, Y. Ma, C. Wang, M. Chen, and Y. Chen, J. Phys. Chem. C **113**, 13103 (2009).

[131] A.T.T. Koh, Y.M. Foong, L. Pan, Z. Sun, and D.H.C. Chua, Appl. Phys. Lett. **101**, 183107 (2012).

[132] A. Malesevic, R. Kemps, A. Vanhulsel, M.P. Chowdhury, A. Volodin, and C. Van Haesendonck, J. Appl. Phys. **104**, 084301 (2008).

[133] S.H. Al-Harthi, a. Karaa, T. Hysen, M. Elzain, a. T. Al-Hinai, and M.T.Z. Myint, Appl. Phys. Lett. **101**, (2012).

[134] J.L. Qi, X. Wang, W.T. Zheng, H.W. Tian, C.Q. Hu, and Y.S. Peng, J. Phys. D. Appl. Phys. **43**, 055302 (2010).

[135] J. Liu, B. Zeng, Z. Wu, J. Zhu, and X. Liu, Appl. Phys. Lett. **97**, 1 (2010).

[136] B.Y. Zhang, T. Liu, B. Meng, X. Li, G. Liang, X. Hu, and Q.J. Wang, Nat. Commun. **4**, 1811 (2013).

[137] F. Xia, T. Mueller, Y.-M. Lin, A. Valdes-Garcia, and P. Avouris, Nat. Nanotechnol. **4**, 839 (2009).

[138] D. Sun, G. Aivazian, A.M. Jones, J.S. Ross, W. Yao, D. Cobden, and X. Xu, Nat. Nanotechnol. **7**, 114 (2012).

[139] N.M. Gabor, J.C.W. Song, Q. Ma, N.L. Nair, T. Taychatanapat, K. Watanabe, T. Taniguchi, L.S. Levitov, and P. Jarillo-Herrero, Science **334**, 648 (2011).

[140] E. Sargent, Nat. Nanotechnol. **7**, 349 (2012).

[141] K. Thiyagarajan, A. Ananth, B. Saravanakumar, Y.S. Mok, and S.J. Kim, Carbon N. Y. **73**, 25 (2014).

[142] K. Thiyagarajan, B. Saravanakumar, and S.-J. Kim, ACS Appl. Mater. Interfaces **7**, 2171 (2015).

[143] R. Narayanan, H. Yamada, M. Karakaya, R. Podila, a. M. Rao, and P.R. Bandaru, Nano Lett. **15**, 3067 (2015).

[144] V. Georgakilas, M. Otyepka, A.B. Bourlinos, V. Chandra, N. Kim, K.C. Kemp, P. Hobza, R. Zboril, and K.S. Kim, Chem. Rev. **112**, 6156 (2012).

List of Figures
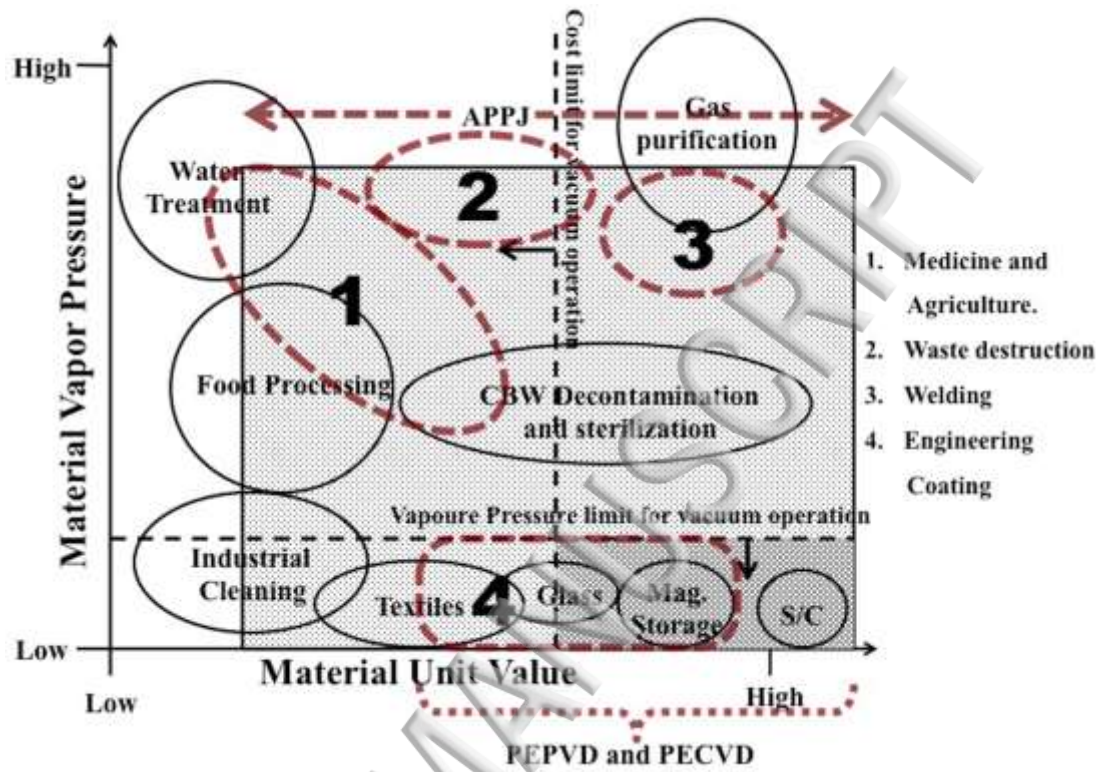
Figure 1. Comparison of the process limits resulting from vapor pressure and economic constraints for both vacuum and atmospheric pressure plasma processing. The rectangular box in the lower right corner represents the domain for vacuum processing. The larger box represents the domain constraints for atmospheric pressure plasma processing. The larger box also contains much of the process domain represented for vacuum based plasma processing. [41] Adapted from Selwyn et al., Contrib. to Plasma Phys. 41, 610 (2001) . Copyright 2001 John Wiley and Sons.
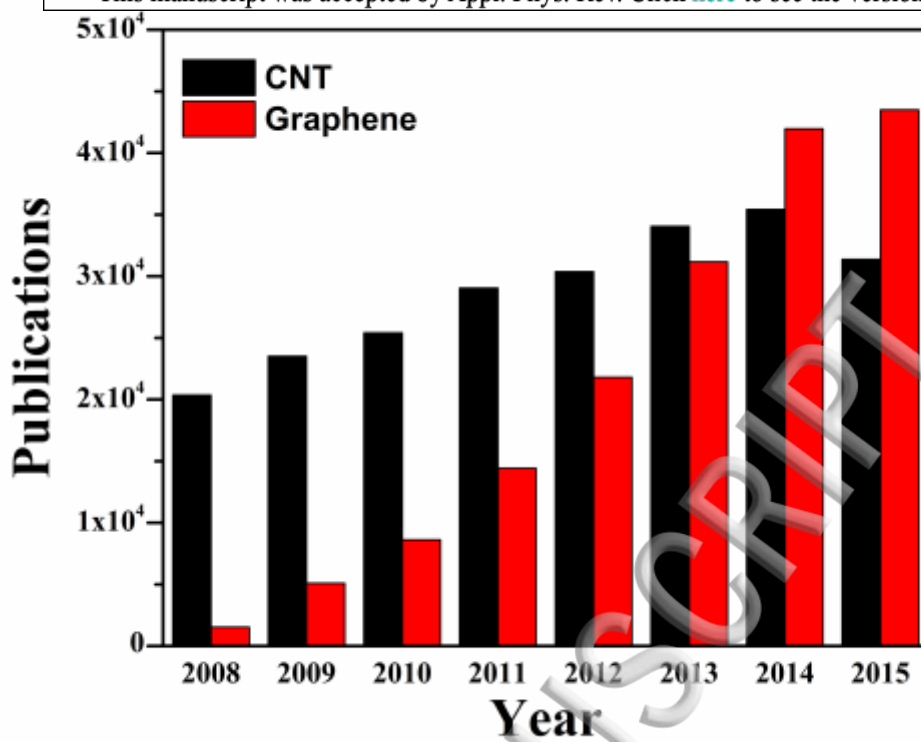
Figure 2. Publication history since 2008. Data taken from Web of Science.
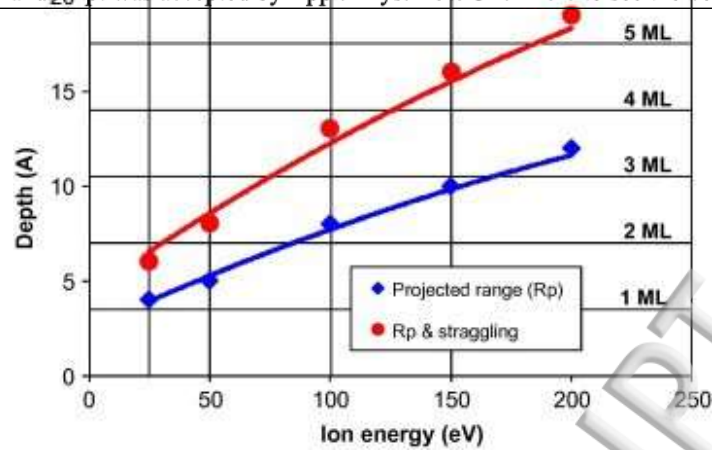
Figure 3. The ion energy dependence of the projected energy range (R_p) representing the mean depth at which the majority of ions of a given energy stop (lower curve) and R_p with the added in-depth straggling (upper curve). Depth in monolayers (ML) indicated at right hand scale. [67] Reprinted with permission from Bertóti,et al., Carbon N. Y. 84, 185 (2015). Copyright 2015 Elsevier.
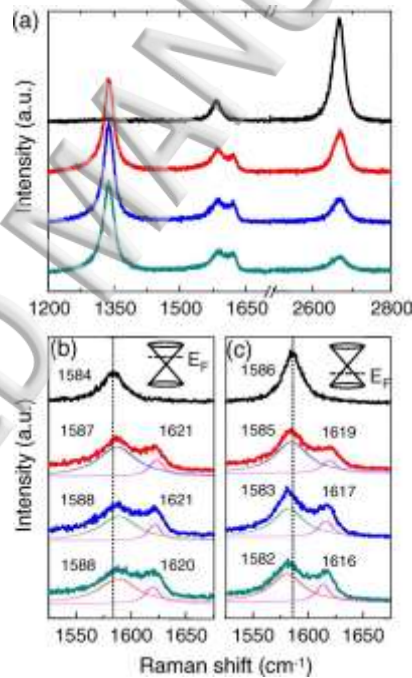
Figure 4. (a) Raman spectra of NH_3 plasma-treated graphene on Ni with different exposure times. The *G* peaks were scaled to have similar intensity. (b) and (c) show the evolution of *G* peak upon plasma exposure for graphene with initial Fermi level lying in conduction band and valance band, respectively. The dashed lines indicate the *G* peak position of pristine graphene.[68] Reprinted with permission from Lin et al., Appl. Phys. Lett. 96, 133110 (2010). Copyright 2010 AIP Publishing LLC.
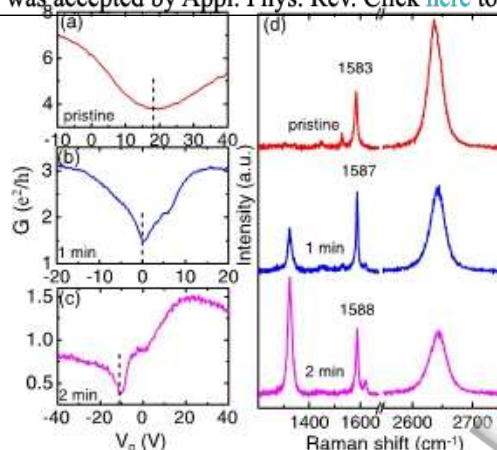
Figure 5.[(a)–(c)] $G_{ds}-V_g$ curves of the same exfoliated graphene at different doping states measured at 10 K. The dashed lines indicate the gate voltage at the charge neutrality point. (d) Raman spectra correspond to the graphene at different doping states shown in [(a)–(c)].[68] Reprinted with permission from Lin et al., Appl. Phys. Lett. 96, 133110 (2010). Copyright 2010 AIP Publishing LLC.
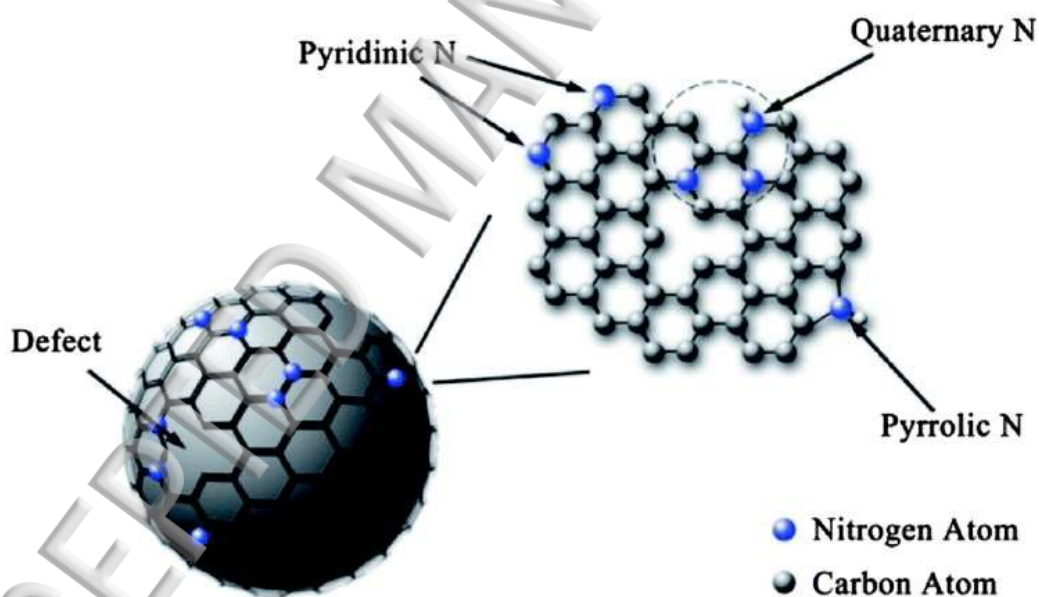
Figure 6. Schematic representation of the N-doped graphene-encapsulated Pt nanocrystal. [75] Reprinted with permission from Ding et al., J. Mater. Chem. A 2, 472 (2014). Copyright 2014 Royal Society of Chemistry.
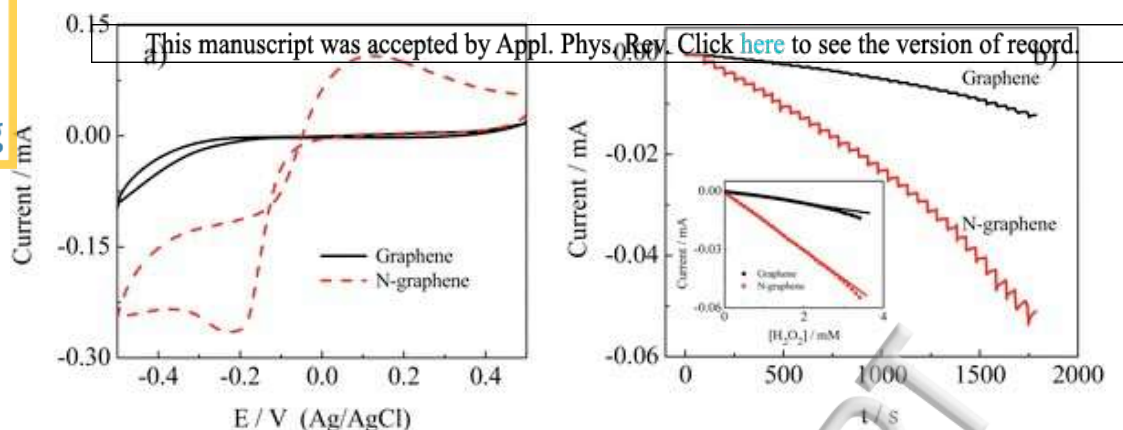
Figure 7. a) CVs (50 mV/s, background-subtracted) of H_2O_2 reduction on graphene and N-graphene in N_2-saturated 5 mM H_2O_2 + 10 mM PBS + 100 mM KCl (pH = 7.4). b) I–t Chronoamperometric responses on graphene and N-graphene at −0.2 V (Ag/AgCl) in N_2-saturated 10 mM PBS + 100 mM KCl (pH = 7.4) with successive addition of 0.1 mM H_2O_2 (inset: calibration curves of H_2O_2 reduction) [78] Reprinted with permission from Shao et al., J. Mater. Chem. 20, 7491 (2010). Copyright 2010 Royal Society of Chemistry.
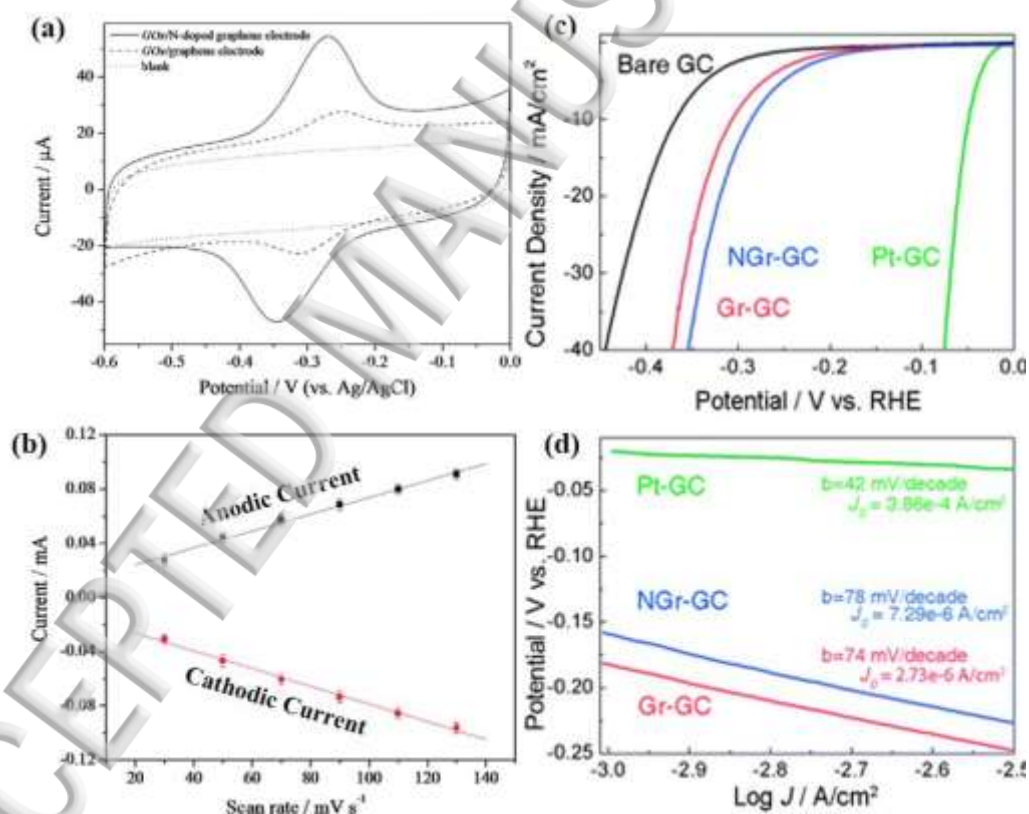
Figure 8. (a) Cyclic voltammograms of GOx immobilized on N-doped graphene electrode and graphene electrode in N_2-saturated 0.1 M PBS solution (pH 7.0). (b) Plot of the anodic and cathodic peak currents from cyclic voltammograms of GO_x versus different scan rate: 0.03, 0.05, 0.07, 0.09, 0.11, 0.13 V/s. [79] (c) CV curve of GC, Gr on GC, NGr on GC, and Pt on GC from a rotating disk electrode system.(d) Tafel plots of different electrode configuration. The 'b' (mV per decade) and J_0 (A cm^{-2}) in the inset indicate a Tafel slope and an exchange current density, respectively [81] Reprinted with permission from (a),(b) Wang et al., ACS Nano 4, 1790 (2010). Copyright 2010 American Chemical Society. (c),(d) Sim et al., Energy Environ. Sci. 6, 3658 (2013). Copyright 2013 Royal Society of Chemistry.
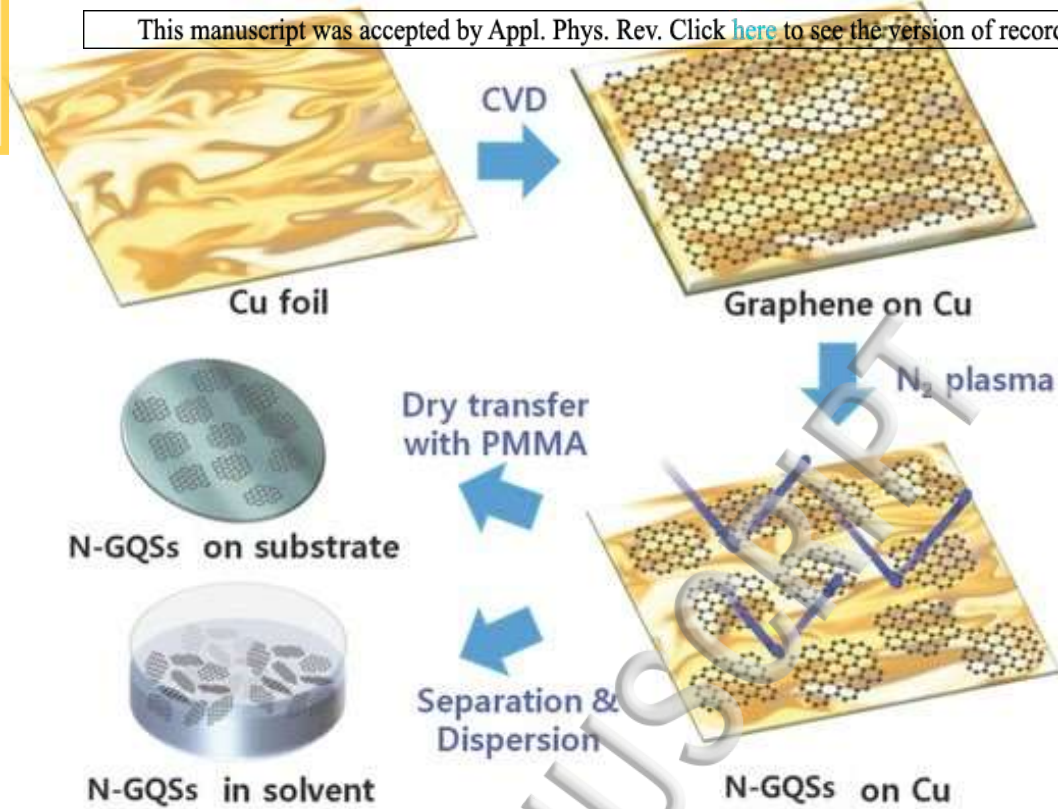
Figure 9. Schematic illustration of N-GQSs fabrication processes. [82] Reprinted with permission from Moon et al., Adv. Mater. 26, 3501 (2014). Copyright 2014 John Wiley and Sons.
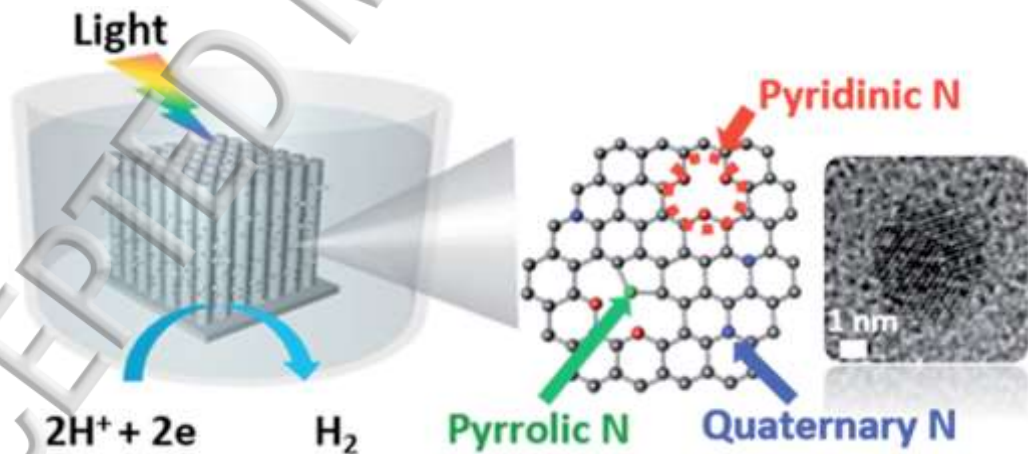
Figure 10.Schematic of N-doped graphene quantum sheets (N-GQSs) decorated on a Si nanowire (SiNW) photocathode electrode. Photons absorbed by the SiNWs generate minority carriers (electrons), which drift to the semiconductor/electrolyte interface, where $2H^+$ is reduced to H_2; the N-GQSs serve as electrocatalysts for hydrogen production. The average diameter of the N-GQSs is 5 nm, as determined from a TEM image [83] Reprinted with permission from Sim et al., Energy Environ. Sci. 8, 1329 (2015). Copyright 2015 Royal Society of Chemistry.
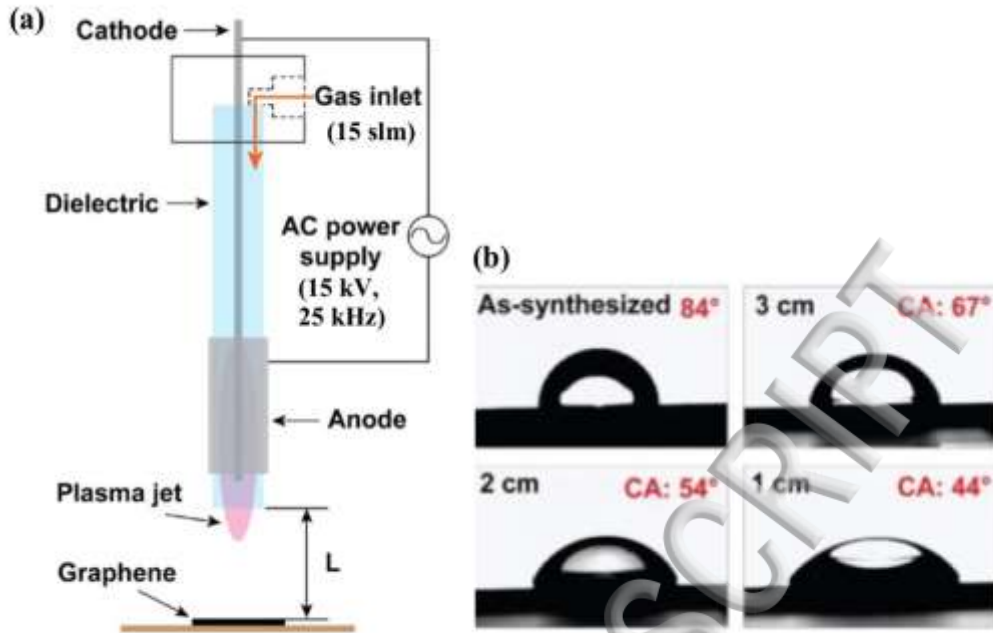
Figure 11. (a) Schematic illustration of the atmospheric pressure plasma jet system (b) Camera images of contact angle measurements for as-synthesized and plasma-treated monolayer graphene with L decreasing from 3 to 1 cm.[92] Reprinted with permission from Lee et al., Curr. Appl. Phys. 15, 563 (2015). Copyright 2015 Elsevier.
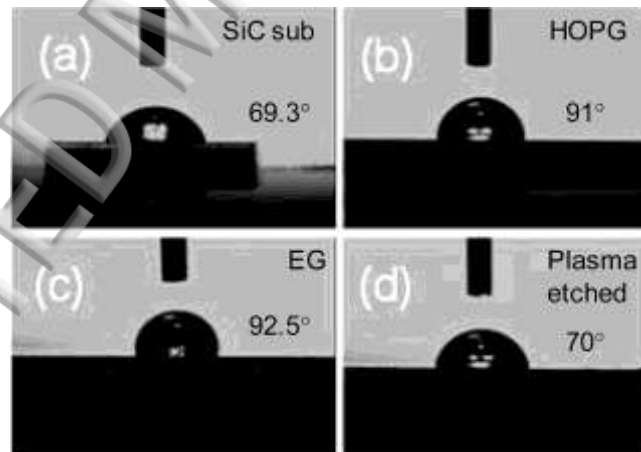
Figure 12. Water droplet on (a) SiC, (b) HOPG, (c) single-layer graphene on SiC, and (d) oxygen-plasma-etched graphene on SiC at 10 W for 2 min. [101] Reprinted with permission from Shin et al., Langmuir 26, 3798 (2010). Copyright 2010 American Chemical Society.
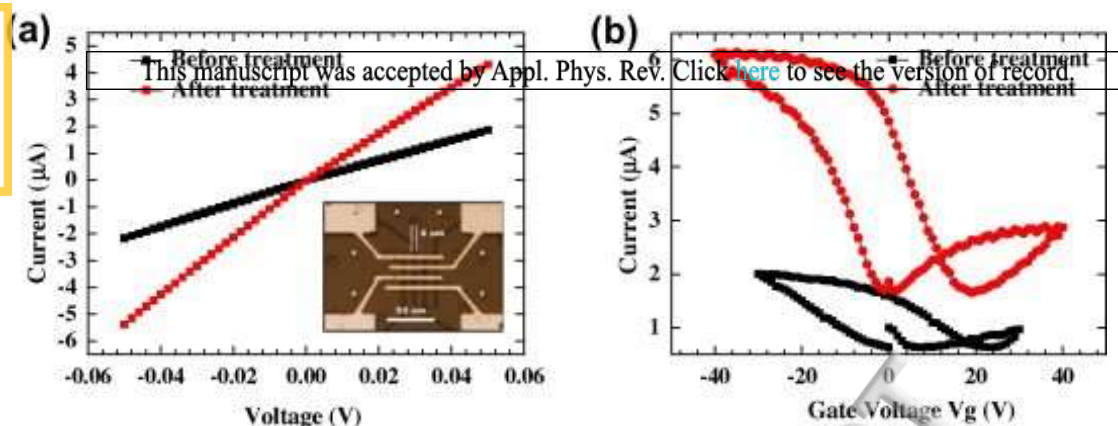
Figure 13. Structured and contacted graphene ribbons, were measured electrically before and after the plasma cleaning treatment. (a) Graphene ribbons have shown linear source–drain current versus bias voltages (I_{ds}–V_{ds}) characteristics and conductivity increased approximately 1.5–6 times after the plasma treatment process. Inset: Structured graphene nanoribbons. (b) Typical ambipolar characteristics, with a higher hole conduction for graphene and hysteresis are observed in both cases. The electron and hole mobilities are increased from 11.2 to 31.9 cm²/V s, respectively to 44.8 and 143.6 cm²/V s with plasma treatment.[104] Reprinted with permission from Peltekis et al., Carbon N. Y. 50, 395 (2012). Copyright 2012 Elsevier.
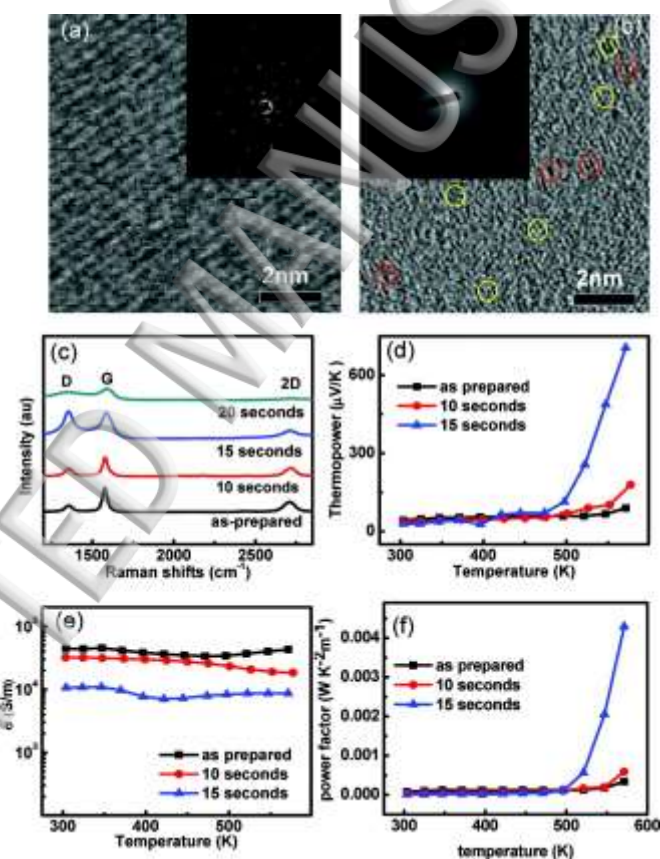
Figure 14. HRTEM images of FLG films (a) before and (b) after oxygen plasma treatment. The corresponding SAED patterns in the inset confirms the loss in crystallinity after oxygen plasma treatment. (c) Raman spectra of the FLG films. (d-f) Temperature- dependent (d) thermopower, (e) electrical conductivity, and (f) power factor for the FLG films after different oxygen plasma treatments.[110]. Reprinted with permission from Xiao et al., ACS Nano 5, 2749 (2011). Copyright 2011 American Chemical Society.
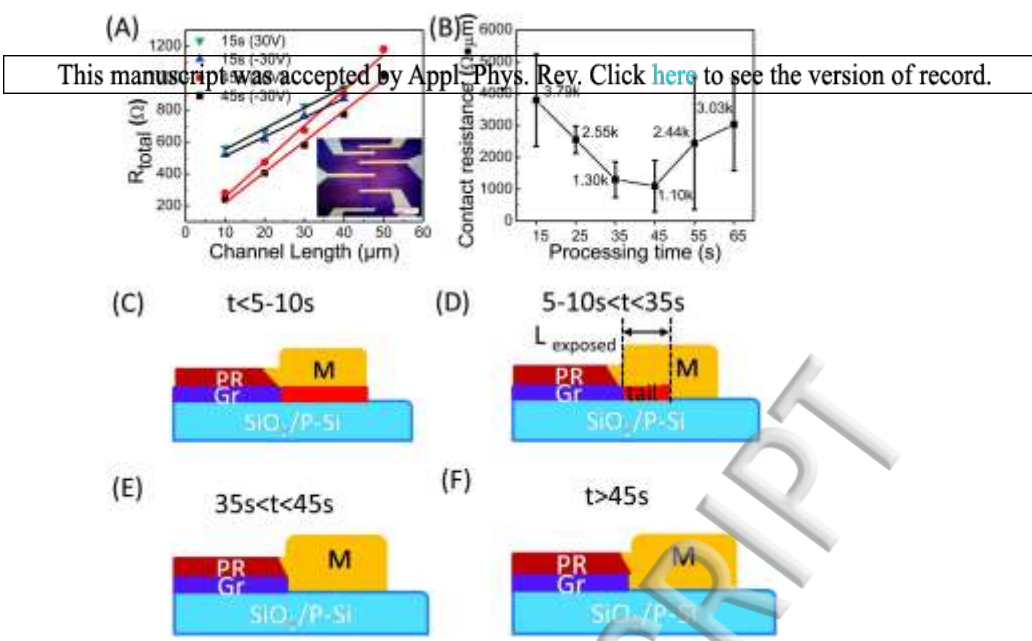
Figure 15. (A) Change in Rc due to plasma treatment for 15 and 45 s and different gate modulation. Inset: optical image of the designed TLM structure with five transistors. (B) Contact resistance versus processing time, showing a large reduction in Rc at 35 to 45s. (C-F) Variation of Graphene edge with plasma treatment. The exposed graphene contact length (L_{exposed}) changed from longer to shorter. [112] Reprinted with permission from Yue et al., Nanoscale 7, 825 (2015). Copyright 2015 Royal Society of Chemistry.
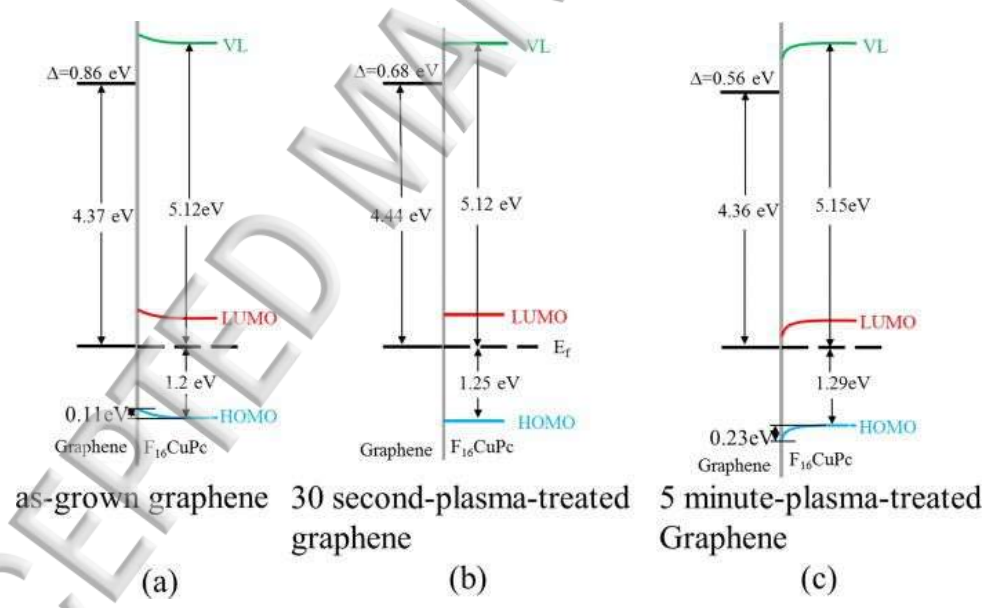
Figure 16. Schematic energy level diagrams of $F_{16}CuPc$ prepared on (a) as grown graphene, (b) 30 seconds plasma-treated graphene; and (c) 5 min plasma-treated graphene. [118] Reprinted with permission from Yang et al., Appl. Phys. Lett. 106, 133502 (2015). Copyright 2015 AIP publishing LLC.

45
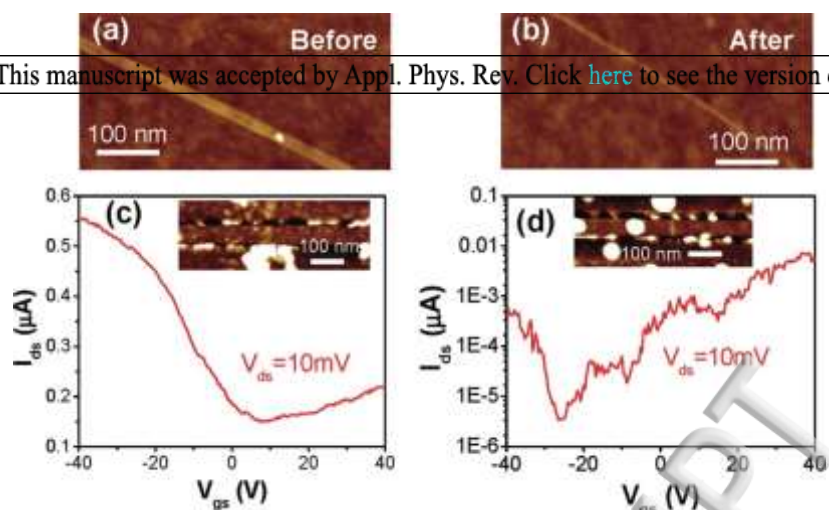
Figure 17. AFM images of a GNR (a) before and (b) after hydrogen plasma for 55 min. Room temperature curves of drain-source current (I_{ds}) to gate-source voltage (V_{gs}) of (c) a GNR (width of ~14 nm) device and (d) a plasma-narrowed device. [120] Reprinted with permission from Xie et al., J. Am. Chem. Soc. 132, 14751 (2010).Copyright 2010 American Chemical Society.
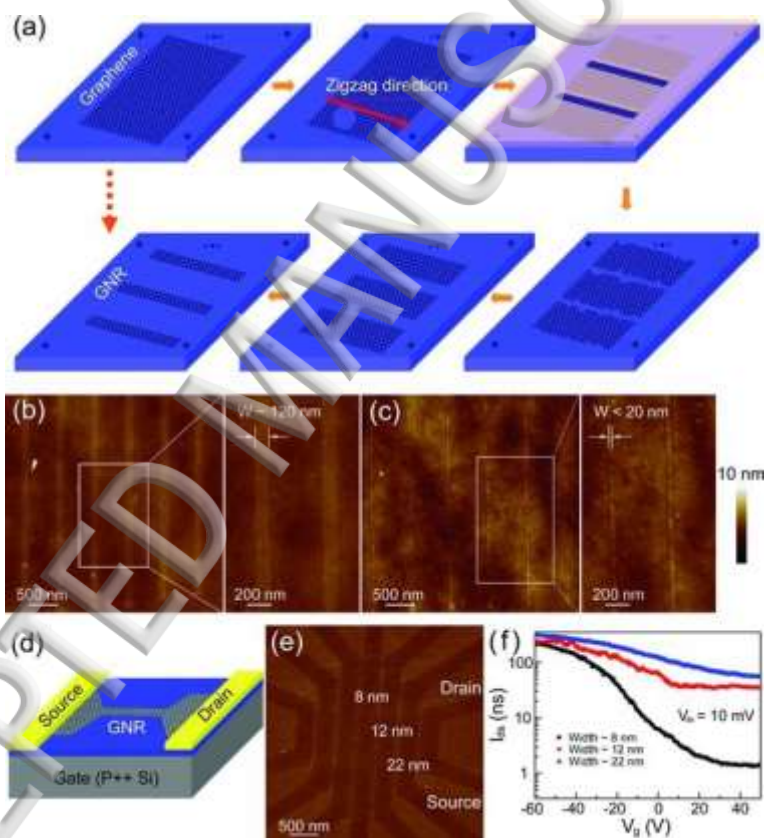
Figure 18. a) Schematic procedures for fabricating a GNR array along a designated crystallographic direction using anisotropic etching. b,c) AFM image for typical graphene patterns generated after O_2 plasma etching and after 50 W H_2 plasma etching at 500 °C for 6 min, respectively. d) Schematic drawing of a GNR-FET using graphene as contact electrodes. e) AFM images of GNR-FETs with different ribbon widths. f) Room-temperature transfer characteristics of GNR-FETs at V_{ds} = 10 mV for three different widths: ≈ 22, ≈ 12, and ≈ 8 nm. [121] Reprinted with permission from Yang et al., Adv. Mater. 22, 4014 (2010). Copyright 2010 John Wiley and Sons.
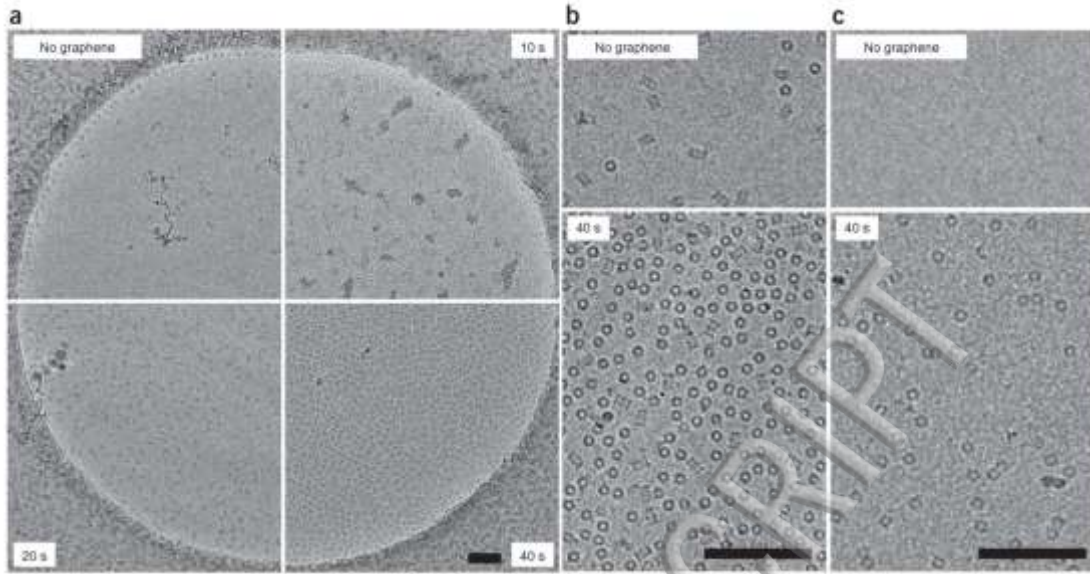
Figure 19. Dose-dependent adsorption of proteins on hydrogen plasma–treated graphene. (a) Cryo-EM micrographs of 70S ribosomes in vitrified ice at 80 K. Upper left quadrant is a standard grid treated with a 10-s hydrogen-plasma dose. The other three quadrants show grids covered with monolayer graphene and treated with 10, 20 or 40 s of hydrogen plasma as indicated. All other sample concentration, blotting, vitrification and imaging conditions are the same for all four grids. Scale bar, 1,000 Å. Electron micrographs of 20S proteasome (b) or apoferritin (c) molecules on graphene treated with 40 s of hydrogen plasma (bottom) and molecules in unsupported ice from an adjacent region of the same grid (top). Scale bars, 1,000 Å. Magnification is the same for b and c. [123] Reprinted with permission from Russo et al ., Nat. Methods 11, 649 (2014). Copyright 2014 Nature Publishing Group.
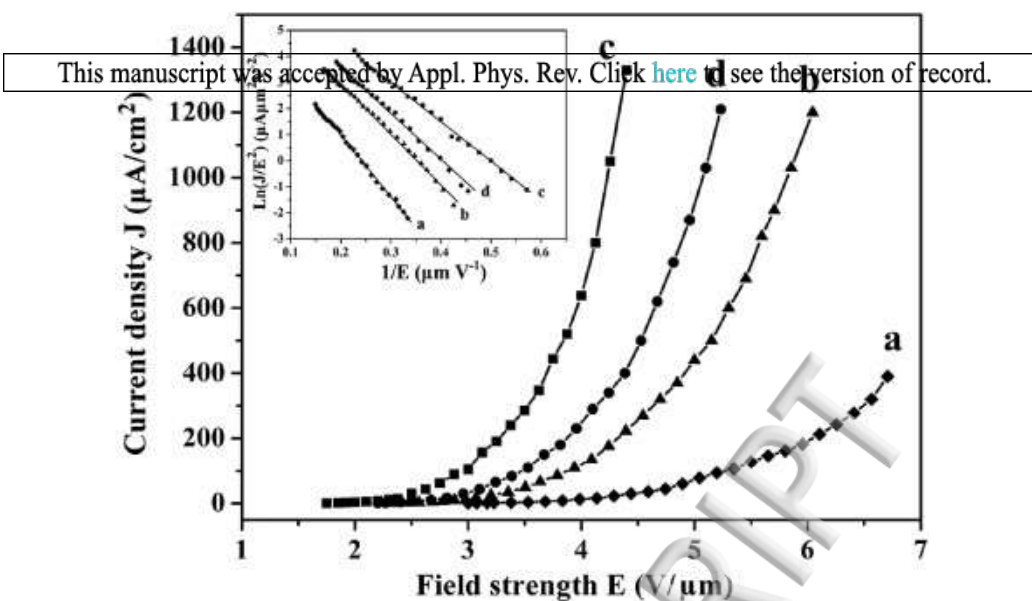
Figure 20. Field emission current density as a function of electric field for the as-grown FLGSs (a) before and (b)–(d) after Ar plasma treatment for 1 min, 3 min and 5 min, respectively, in which the inset exhibits the F–N plots, corresponding to curves a, b, c and d, respectively. Reprinted with permission from Qi et al., J. Phys. D. Appl. Phys. 43, 055302 (2010).Copyright 2010 IOP Publishing.
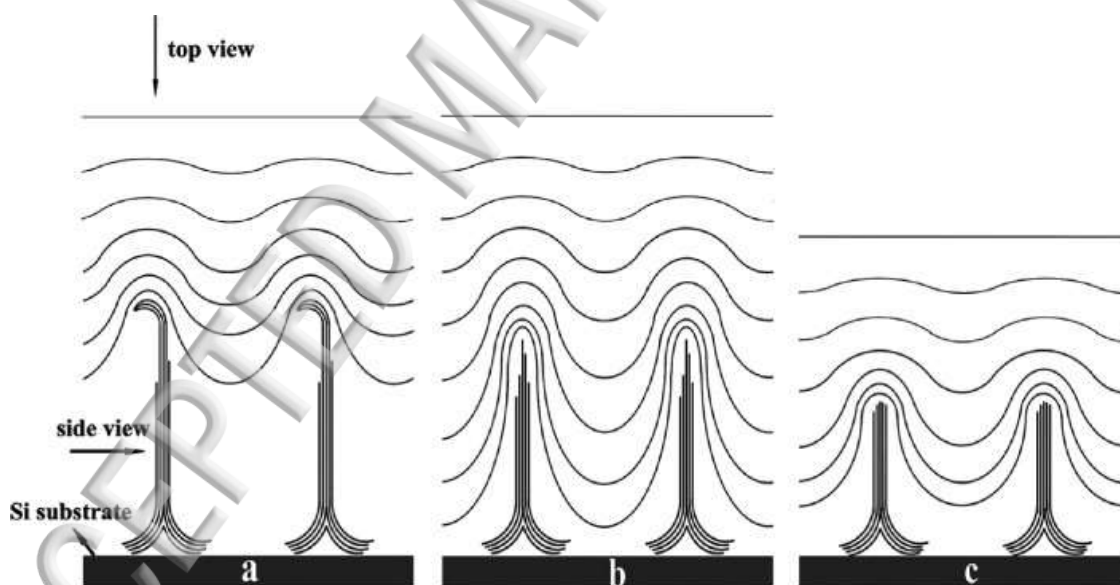
Figure 21. Schematic equipotential model of the as-grown FLGS structure (*a*) before and after Ar plasma treatment for (*b*) 3 min and (*c*) 5 min, respectively.[134] Reprinted with permission from Qi et al., J. Phys. D. Appl. Phys. 43, 055302 (2010).Copyright 2010 IOP Publishing.

48
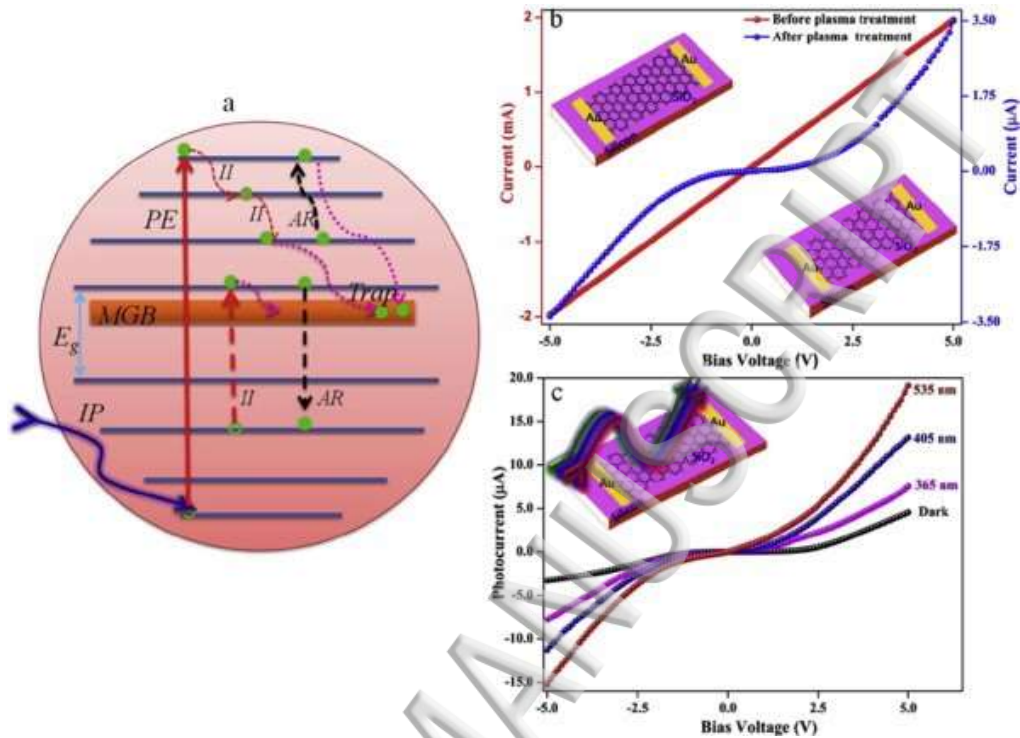
Figure 22. (a) Energy band diagram (including the defect midgap states band (MGB) and band gap energy (Eg), including the concept for photocurrent generation for p-FLG. An incident photons (IP) interacts with the electron in the valence band and generates an electron–hole pair via photon excitation (PE), followed by the impact ionization (II) process. When the excited electron transfers to the lower energy level in the conduction band and transfers the energy to another electron, initiating the AR process. Each of the steps in this cascade increases the population of electron–hole pairs; the multiexcitation generation (MEG) effect exists, possibility of more excited electrons being trapped by the MGB. (b) Current (*I*) versus voltage (*V*) curve for FLG, before (red) and after (blue) plasma irradiation; the insets are the corresponding device structures before (top-left) and after (lower-right) plasma irradiation. (c) The photoresponse *I–V* curve of the p-FLG device under dark conditions and also with various light sources. The inset shows a schematic diagram of the p-FLG device interacting with light source.[141] Reprinted with permission from Thiyagarajan et al., Carbon N. Y. 73, 25 (2014).Copyright 2014 Elsevier.

List of tables

Counter Electrode	Irradiation	J_{sc} (mA/cm^2)	V_{OC} (V)	FF (%)	η (%)	η_{rear} / η_{front}
N-G	Front	13.24	0.713	33	3.12	0.83
	Rear	10.63	0.717	34	2.59	
Pt	Front	14.05	0.717	65	6.55	0.58
	Rear	8.32	0.73	64	3.80	

Table 1. Photovoltaic performances of DSSCs with N-G-40 and Pt CEs under the front and rear side irradiation CEs.[90] Reprinted with permission from Yang et al., Electrochim. Acta 173, 715 (2015). Copyright 2015 Elsevier.

Counter electrode	open-circuit voltage, V_{OC} (V)	short-circuit current density, J_{SC} (mA/cm^2)	fill factor, FF(%)	efficiency, η (%)
Pt	0.73	11.80	65.75	5.65
furnace rGO	0.73	11.50	62.25	5.19
untreated rGO	0.71	1.88	14.29	0.19
APPJ rGO 1 s	0.68	8.81	19.03	1.14
APPJ rGO 5 s	0.72	10.29	57.36	4.28
APPJ rGO 9 s	0.72	11.13	57.09	4.60
APPJ rGO 11 s	0.73	11.11	63.82	5.19
APPJ rGO 13 s	0.69	11.07	58.48	4.48
APPJ rGO 17 s	0.66	8.76	39.95	3.01
APPJ rGO 2 min	0.67	0.99	12.15	0.08

Table 2. Photovoltaic Parameters of DSSCs with Pt and rGO Counter Electrodes Treated by Various Methods. [93] Reprinted with permission from Liu et al., ACS Appl. Mater. Interfaces. 6, 15105 (2014). Copyright 2014 American Chemical Society.

Power in Watts	C_{meas} in $\mu F/cm^2$	C_{SC} $\mu F/cm^2$	C_Q $\mu F/cm^2$	$n_{2d,0}$ ($\times 10^{12}$) cm^{-2}	n ($\times 10^{19}$) cm^{-3}	v_F ($\times 10^6$) m/s	E_F meV
0	1.9 ± 0.7	2.5	9.1	4.5	1.0	1.00	247
5	2.3 ± 0.3	3.2	11.0	7.1	1.9	0.97	302
10	4.3 ± 0.7	7.3	20.3	37	22	0.95	669
20	4.7 ± 0.7	8.4	23.1	43	29	0.86	661
35	4.0 ± 0.3	6.6	19.6	28	15	0.87	533
50	3.1 ± 0.5	5.0	14.2	19	8.5	1.10	562

Table 3. Variation of Measured Capacitance (C_{meas}) of the Few-Layer Graphene with Plasma Power. Which was deconvoluted to yield the Space-Charge Capacitance (C_{SC}) and the Quantum Capacitance (C_Q) with corresponding values of two-dimensional carrier density ($n_{2D,0}$), volumetric charge density (n), Fermi-velocity (v_F) and the Fermi energy (E_F). [143] Reprinted with permission from Narayanan et al., Nano Lett. 15, 3067 (2015). Copyright 2015 American Chemical Society.

			Plasma					
S. No.	**Graphene Type**	**Species/ Element**	**Generation**	**Time**	**Parameters**	**Characteristic changes**	**Application**	**Ref**
1	Mechanically exfoliated	NH_3	Grid- assisted diffusion plasma reactor	10 min	13.56 MHz, 0.1 Torr, 20 Watt , 750 mm distance between the electrodes.	Controlled edge functionalization.	Electronics	69
2	CVD	Ar and NH_3 (5% by flow)	Electron beam generated plasma	60 secs	2keV electron beam, 2 ms pulse width, 20 ms period	Higher signal to noise ratio in BioFET device.	DNA attachment	70
3	CVD	N_2 (50SCCSM)	Rf Plasma	5 min	70 W , base pressure of 2.7×10^{-4} Pa ,working pressure 0.7 Pa	work function from 4.91 eV to 4.37 eV	Electronics	71
4	Chemical exfoliation	N_2	Rf Magnetron sputtering system	30 min	13.56 Mhz, 130 W ,0.1 mBar chamber pressure	Increased electrical conductivity between carbon and catalyst	ORR	74
5	Chemical exfoliation	N_2	Rf Magnetron sputtering system	30 min	13.56 Mhz, 130 W ,0.1 mBar chamber pressure	Enhanced interaction between graphene and metal *d* orbitals	H_2 Storage	77

6	Chemical exfoliation	N$_2$	Harrick model PDC-32G plasma cleaning unit	20,40, 60,100 min	750 mTorr. Plasma power 100 W	Enhanced electron transfer efficiency	Glucose biosensing	79
7	Chemical exfoliation	N$_2$ (91 sccm)	PECVD	1-3 min	14 Torr, 500 W	~280 F/g	Ultracapacitor	84
8	CVD	N$_2$	DC plasma chamber	20,40 secs	300 ~ 350 V negative bias, 460 Pa	Increase in number of active sites after plasma treatmnet	Bifacial DSSC	90
9	CVD	N$_2$ (25 slm)	APPJ	1 to 30 secs	15 kv , 25 kHz	Hydrophobic to hydrophilic, N doping with minimum structural damage	Electronics	92
10	Micromechanical exfoliation	O$_2$	Parallel plate rf plasma System	3 sec	13.57 MHz, 15 W(50 mW/cm^2 power density), 20 mTorr	Band gap opening	Optoelectronics	95
11	Chemical exfoliation	O$_2$	Cesar 133 RF power generator	10 sec	13.56 MHz, 200 W , 100 Pa pressure	Increased response towards electrochemical activity	Graphene film Actuator	102
12	CVD	O$_2$	Microwave radical generator	2 min	1000 W DC power ,1 Torr, 100 sccm O$_2$ flow	Cleaning polymer residue after transfer.	Electronics	104

13	CVD	O_2/Ar (1:10)	Harrick model PDC-32G plasma cleaning unit	10,15,20 sec	6.8 W input power	Increased thermo power	Thermo electric effect	110
14	Chemical exfoliation	O_2	Capacitively coupled plasma	1 - 5 min	120 mTorr chamber pressure, 25−200Wpower, substrate reflective frequency of 13.56 MHz	Patterning	Flexible transparent electrodes	113
15	CVD	O_2	Parallel plate rf plasma System	5 sec – 2 min	13.57 Mhz, , 2-5 W,0.15 mBar chamber pressure	O_2 induced lattice dipole, downshift of E_F	SERS, Molecular sensing	115
16	CVD	Ar/H_2 (85/15) 200 sccm	Reactive ion etching system		13.56 Mhz, 3 W(power density is 4 mW/cm^2),0.05 mBar chamber pressure	Reversible Hydrogenation	Electronics	117
17	Peel-off	H_2	Tube furnace with rf plasma source	60 min	300 °C, 300mTorr H_2 pressure, 20 W plasma power	Selective etching at the edges	FET with high on/off ratio	120
18	CVD	H_2	Rf plasma (Fischione 1070)	10,20,40 sec	13.56 Mhz, 10^{-6} mBar chamber pressure	Uniform protein distribution	Cryo em grids	123
19	PECVD	Ar (10 sccm)	Rf plasma	1,3,5 min	800 °C, 150Pa and 150W	Decreases the turn-on electric field and increase in the maximum emission current density	Graphene field emission devices	135

54

| 20 | Peel -off | Ar (60 sccm) | Atmospheric pressure plasma reactor | 1 min | 1 Torr, 130 V | Tunable photoresponse | Photodetector | 142 |

Table 4. Overview of the review showing broad applicability of plasma engineered graphene.

Legend:
- ● Projected range (Rp)
- ● Rp & straggling

Axes: Depth (Å) vs Ion energy (eV); data labeled 1 ML, 2 ML, 3 ML, 4 ML, 5 ML

(a)

Intensity (a.u.)

1200 1350 1550 2600 2700 2800

(b)

1584

E_g

Intensity (a.u.)

1587   1621
1588   1620
1588   1620

1550   1600   1650
Raman shift (cm⁻¹)

(c)

1586

E_g

1585   1619
1583   1617
1582   1616

1550   1600   1650
Raman shift (cm⁻¹)

Pyridinic N

Quaternary N

Defect

Pyrrolic N

● Nitrogen Atom
● Carbon Atom

a)

b)

(a)
- GCh7N-doped graphene electrode
- GCh/graphene electrode
- blank

(b)
- Anodic Current
- Cathodic Current

(c)
- Bare GC
- NGr-GC
- Gr-GC
- Pt-GC

(d)
- Pt-GC: b=42 mV/decade, $J_0 = 3.86e-4$ A/cm^2
- NGr-GC: b=78 mV/decade, $J_0 = 7.29e-6$ A/cm^2
- Gr-GC: b=74 mV/decade, $J_0 = 2.73e-6$ A/cm^2

CVD

Cu foil

Graphene on Cu

N₂ plasma

N-GQSs on substrate

Dry transfer with PMMA

N-GQSs in solvent

Separation & Dispersion

N-GQSs on Cu

Light

Pyridinic N

Pyrrolic N

Quaternary N

1 nm

$2H^+ + 2e$ H_2

(a) Cathode / Gas inlet (15 slm) / Dielectric / AC power supply (15 kV, 25 kHz) / Anode / Plasma jet / Graphene / L

(b) As-synthesized CA: 84° / 3 cm CA: 67° / 2 cm CA: 54° / 1 cm CA: 44°

(a) SiC sub 69.3°
(b) HOPG 91°
(c) EG 92.5°
(d) Plasma etched 70°

(a) Current (μA) vs Voltage (V)
— Before treatment
— After treatment

(b) Current (μA) vs Gate Voltage Vg (V)
— Before treatment
— After treatment

(a)

(c)
Intensity (au)

D   G   2D

20 seconds

15 seconds

10 seconds

as-prepared

1500   2000   2500
Raman shifts (cm^{-1})

(d)
Thermopower (μV/K)

- as prepared
- 10 seconds
- 15 seconds

300   400   500
Temperature (K)

(e)
σ (S/m)

- as prepared
- 10 seconds
- 15 seconds

300   400   500
Temperature (K)

(f)
power factor (W K^{-2} m^{-1})

- as prepared
- 10 seconds
- 15 seconds

300   400   500   600
temperature (K)

(A) R_{Total} (Ω) vs Channel Length (μm) — 15s (30V), 15s (-30V), 45s (30V), 45s (-30V)

(B) Contact resistance (Ω) vs Processing time (s) — 3.79k, 2.55k, 1.30k, 1.10k, 2.44k, 3.03k

(C) t<5-10s
(D) 5-10s<t<35s, $L_{exposed}$, tail
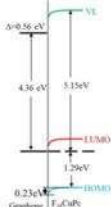(E) 35s<t<45s
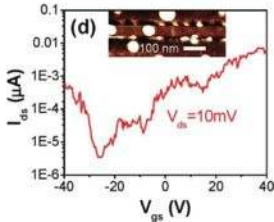(F) t>45s

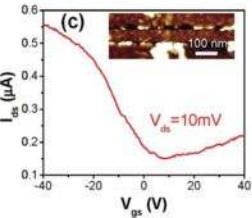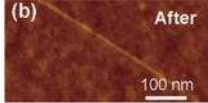PR — Gr — M — SiO$_2$/P-Si

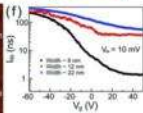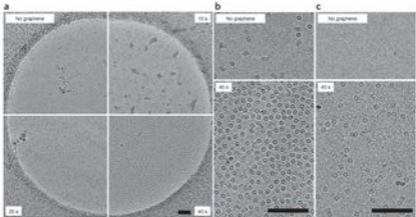| (a)	(b)	(c)
as-grown graphene	30 second-plasma-treated graphene	5 minute-plasma-treated Graphene

Figure labels:

(a) as-grown graphene
Δ=0.86 eV — VL
4.37 eV   5.12 eV
LUMO
1.2 eV
0.11eV — HOMO
Graphene $F_{16}CuPc$

(b) 30 second-plasma-treated graphene
Δ=0.68 eV — VL
4.44 eV   5.32 eV
LUMO
E_F
1.25 eV
HOMO
Graphene $F_{16}CuPc$

(c) 5 minute-plasma-treated Graphene
Δ=0.56 eV — VL
4.36 eV   5.15 eV
LUMO
1.29eV
0.23eV — HOMO
Graphene $F_{16}CuPc$

(a) Before — 100 nm

(b) After — 100 nm

(c) I_{ds} (µA) vs V_{gs} (V), V_{ds}=10mV, 100 nm

(d) I_{ds} (µA) vs V_{gs} (V), V_{ds}=10mV, 100 nm

(a) Graphene / Zigzag direction / GNR

(b) W ~ 120 nm / 500 nm / 200 nm

(c) W < 20 nm / 500 nm / 200 nm

(d) Source / Drain / GNR / Gate (P++ Si)

(e) 8 nm / 12 nm / 22 nm / Drain / Source / 500 nm

(f) Width = 8 nm / Width = 12 nm / Width = 22 nm / V_{ds} = 10 mV

top view

side view

Si substrate